Tailoring mechanical properties of a multi-principal element alloy through a multi-length-scale approach

Chang-Yu Hung[1,2,*], Milan Heczko[3], Chenyang Li[4], Dallin J. Barton[5], Paul D. Jablonski[1], Wei Chen[4], Arun Devaraj[6], Michael J. Mills[3], Martin Detrois[1], Stoichko Antonov[1]

[1] National Energy Technology Laboratory, 1450 Queen Avenue SW, Albany, OR 97321, USA
[2] NETL Support Contractor, 1450 Queen Avenue SW, Albany, OR 97321, USA
[3] Department of Materials Science and Engineering, The Ohio State University, 2041 College Road, Columbus, OH 43210, USA
[4] Department of Materials Design and Innovation, University at Buffalo, The State University of New York, Buffalo, NY, 14260, USA
[5] National Security Directorate, Pacific Northwest National Laboratory, Richland, WA, USA
[6] Physical and Computational Sciences Directorate, Pacific Northwest National Laboratory, Richland, WA, USA

**Corresponding author: Email address: cyhung916.tw@gmail.com*
Address: National Energy Technology Laboratory, 1450 Queen Avenue. SW, Albany, OR 97321, USA

Abstract

In this study, a multi-length-scale strengthening approach was used to tailor the microstructure and the mechanical properties of a NiCoCr-based multi-principal element alloy (MPEA). Grain size refinement, severe lattice distortion, and stacking fault energy (SFE) reduction with Mo addition (up to 10 at.%) enhance yield strength by 85% with only 10% reduction in ductility in as-annealed MPEAs. A pronounced increase in the strain hardening rate was observed with the addition of Mo, which is ascribed to the promotion of complex stacking fault (SF) interaction and intersection, accompanied by Lomer-Cottrell (L-C) and Hirth locks inhibiting dislocation motion and substantial increase in the accumulation of back stress. To push the limit of the yield strength further, the Suzuki segregation phenomenon was manipulated by a careful control of SF density by pre-straining and a subsequent 500 °C heat treatment. The stress-strain responses of the pre-strained and heat treated MPEAs showed an obvious SF density and Mo concentration dependence. The yield strength of the pre-strained Mo-added MPEAs with subsequent heat treatment was increased up to true stress of 2.3 GPa with a corresponding fracture elongation of 12% true strain. SFs formed during pre-straining served as Cr segregation sites during subsequent heat treatment, which substantially varies the local SFE within the SF, presenting a roughened landscape and frustrating the dislocation dynamics. Beyond conventional strengthening strategies, incorporation of refractory elements along with the manipulation of Suzuki segregation process provide a promising route in tailoring desired mechanical properties of MPEAs.

Keywords: Multi-principal element alloys, Mechanical properties, Stacking fault, Suzuki segregation, Molybdenum

1. Introduction

Some multi-principal element alloys (MPEAs), including equiatomic, single-phase CrCoNi [1–3] and CrCoFeMnNi [4–6], are now widely recognized for their remarkable combinations of pronounced hardening rates, high ductility, and exceptional fracture toughness at room and cryogenic temperatures. The pronounced strain hardening regulating the balance between strength and ductility has undergone extensive research, but the governing mechanisms are still up for debate [7–11]. So far, the mechanisms that have been put forth regarding the strain hardening rate are related to an increase in lattice distortion [9,12,13] and a decrease in stacking fault energy (SFE) [14–17]. Lattice distortion is a fundamental characteristic of MPEAs. Given the local chemical environment, each atom's bonding environment may differ from that of the average lattice site, which also provides higher lattice friction stress upon deformation of MPEAs compared to pure metals. On the other hand, a significant reduction in SFE promotes dislocation dissociation into a/6<112> Shockley partial dislocations bound by an intrinsic stacking fault (ISF) at low strain. Further deformation results in the development of more complex defect configurations such as extrinsic stacking faults (ESF) and nano-sized deformation twins. Moreover, a highly localized phase transformation can also occur where the bands of hexagonal close-packed (HCP) crystal structure act as strong obstacles to the motion of non-coplanar dislocations, thus increasing macroscopic hardenability [18]. Twinning-induced plasticity (TWIP) and transformation-induced plasticity (TRIP) observed in MPEAs can be analogous to several studies in advanced austenitic steels [16,19–21].

Although significant efforts have been made to understand the fundamental mechanisms governing the strength-ductility trade-off relationship in some MPEAs, the yield strength of single-phase face-centered cubic (FCC) MPEAs with recrystallized structure remains insufficient, thus limiting their structural applications. Several approaches have been attempted and have achieved early success in overcoming the drawbacks of low yield strength, such as grain size refinement [22–24], precipitation strengthening [25–28], and inducing a heterogeneous microstructure [29,30]. Tsuji et al. [31] suggests that a reduction of grain size down to submicron regimes in low-SFE alloys successfully enables high yield strength and large ductility by sequential nucleation of different deformation modes. Sohn et al. [12] reported on a simple VCoNi equiatomic medium-entropy alloy that exhibits a near 1 GPa yield strength and good ductility by introducing severe lattice distortion. Given the well-known strengthening strategies mentioned above, lattice distortion and grain boundary hardening (through grain size refinement) are two fundamental mechanisms for improving yield strength. At the same time, ductility enhancement generally requires the activation of alternative deformation modes, such as deformation twinning or phase transformation in response to the extensive flow stresses.

The segregation of solute atoms to planar faults, mainly stacking faults (SFs), has been shown to inhibit the subsequent motion of dislocations and can be utilized to enhance the resistance of an alloy to plastic deformation; this has been studied in CoNi-based superalloys [32–34] and CoCrFeNi-based high-entropy alloys (HEAs) [35]. This enrichment of solute atoms at SFs was first observed by Suzuki in 1962 [36], but it has only recently been explored as a potent strengthening mechanism. Due to the chemical complexity of MPEAs, i.e., each element has a concentration higher than 5%, these alloys pose an interesting opportunity for Suzuki segregation and a resultant hardening behavior. A study on modified CoCrFeNi-based HEA explored this mechanism [35]. The alloy was heavily cold-rolled and subsequently aged at 500 °C, and the authors claim that the enrichment of Co solute segregating at SFs gives rise to an increment of high yield strength. This suggests that the degree of Suzuki hardening can be potentially tuned with careful control of SFs density and alloy composition in addition to conventional strengthening strategies such as grain size refinement and solid solution hardening.

This study aims to tailor the mechanical properties of a class of MPEAs by conventional strategies together with Suzuki segregation. Hence, a multi-length-scale approach can be carried out as follows: First, conventional strengthening strategies i.e., grain size refinement, solid solution strengthening, and SFE reduction, can be achieved by alloying with refractory element. Second, the density of lattice defects, mainly SFs, is carefully controlled through pre-straining. This is finally followed by the third step involving heat treatment which facilitates the effects of Suzuki segregation in relation to the defect network established during previous processing step. The base alloy chosen for the investigation is $Ni_{35}Co_{35}Cr_{(30-x)}Mo_x$, with small Mo additions from 0 at.% up to 10 at.% substituting for Cr. Our hypothesis posits that the incorporation of Mo not only increase lattice distortion owing to Mo's larger metallic radius compared to that of Co, Cr, and Ni elements [13,36,37], but also reduce SFE that facilitates the formation of SFs for elemental segregation [13,37,38]. Mechanical assessments of these alloys are conducted in two conditions: (i) in an as-annealed state, and (ii) after pre-straining followed by 500 °C heat treatment. This report demonstrates that the Mo partitioning and Suzuki hardening can be finely tuned to attain a wide range of mechanical properties. Specifically, one of the studied alloys deformed in tensile loading to a true strain of 0.47, exhibits a pronounced increment in true stress of 2.3 GPa while maintaining large ductility of 12% post heat-treatment.

2. Experimental details

2.1 Sample fabrication

The alloys were manufactured using vacuum induction melting (VIM) from high-purity industry grade melt stock. The melt charges weighted 8 kg and were loaded in an alumina crucible for VIM under 200 Torr (26.7 kPa) partial pressure of argon. Once melted, the liquid metal was brought to a 50 °C superheat and poured into a cylindrical graphite mold to form 75 mm diameter ingots. The ingots were homogenized in a vacuum heat-treatment furnace with high-vacuum capabilities and utilizing a 50 Torr (6.7 kPa) argon partial pressure once the heat treatment temperature reaches 800 °C. A computationally optimized heat treatment schedule was determined based on chemistry and microstructure to reduce residual elemental inhomogeneity to below 1%. Hot working was performed at 1100 °C and consisted of steps of forging followed by hot rolling with reheating between each step. Doing so, the ingots were processed into ~10 mm thick plates.

2.2 Mechanical testing

The rolled plates that had undergone the aforementioned thermomechanical processing scheme were used to create the tensile testing specimens, which were cut so that the tensile axis was parallel to the rolling direction. The samples were cylinder-shaped bars with an overall length of 76.2 mm, gauge section length of 31.75 mm, and reduced diameters of 6.25 mm. Tensile testing was performed at room temperature using an Instron 5900R with 100 kN load cell. The crosshead displacement rate was initially 0.127 mm/min (6.7×10^{-5} s^{-1}) until 1.2% elongation after which the crosshead displacement rate was increased to 1.27 mm/min (6.7×10^{-4} s^{-1}) through failure. The crosshead displacement rate for the loading-unloading-reloading (LUR) tests was 1.27 mm/min (6.7×10^{-4} s^{-1}). At a certain unloading strain, the specimen was unloaded in a load-control mode to 200 N at an unloading rate of 1.27mm/ min (6.7×10^{-4} s^{-1}), followed by reloading to the same applied load.

2.3 Microstructure characterization

The as-annealed and pre-strained and heat-treated samples were characterized with a JEOL-IT700 scanning electron microscope (SEM) using back-scattered electron (BSE) imaging mode as well as the electron back-scattered diffraction (EBSD) detector from Oxford Instruments. The EBSD maps were acquired with an acceleration voltage of 20 kV with a working distance of 15 mm. The samples were scanned with step size of 500 nm. No data clean-up was performed except for the removal of some points with low confidence index values.

For examination using transmission electron microscopy (TEM), the bulk specimens were cut into the 3 mm discs, which were subsequently physically reduced to 70 μm thickness. Electron-transparent specimens were obtained using a Struers TenuPol-5 twin-jet electropolisher with a 20% Perchloric acid and 80% Ethanol electrolyte solution at 16 °C and an applied voltage of 20 V.

Overall microstructure and defect analysis was performed using a JEOL 2100Plus scanning transmission electron microscope (STEM) at an accelerating voltage of 200 kV. Advanced multi-scale characterization down to the atomic resolution was achieved with the S-CORR probe aberration-corrected and mono-chromated Thermo Fisher Scientific (TFS) Themis-Z STEM at an accelerating voltage of 300 kV. STEM diffraction contrast imaging (DCI) was performed with bright (BF) and high-angle annular dark-field (HAADF) detectors by selection of the appropriate camera length [39]. Atomic resolution imaging of the microstructure was performed by tilting of the thin foils into specific low-index crystallographic zones. Data were collected and processed using TFS Velox software. STEM micrographs were corrected for potential sample drift and scanning beam distortions using the drift-corrected frame integration function of Velox. Center of Symmetry (COS) analysis, which determines the degree of centro-symmetry for each atomic column in the experimental HAADF-STEM image and thus identifies distortions in the stacking sequence, was performed according to the procedure described in Refs. [40,41].

Site-specific specimens containing stacking faults were prepared for atom probe tomography (APT) analysis using focused ion beam (FIB) lift-out techniques and annular milling with a Thermo Fisher Scientific Helios 600 Ga^+ FIB. The APT analysis was conducted using a CAMECA LEAP 5000 XR APT. The temperature of the sample during APT data acquisition was maintained at 40 K. Data was acquired via laser-assisted field evaporation. The energy of the laser pulse was nominally 20 pJ pulsing at 200 kHz and the evaporation rate was maintained at 0.005 atoms/pulse. The data obtained from APT was reconstructed and analyzed using the AP Suite software (version 6.3.3.7) from CAMECA instruments.

2.4 First-principles calculations

The Exact Muffin-Tin Orbital (EMTO) [42–45] method is an enhancement of the Koringa-Kohn-Rostoker (KKR) approach, which employs optimized overlapping muffin-tin potential spheres to precisely represent the one-electron potential. To describe the chemical disorder of the high-entropy alloy system, this EMTO method can be combined with coherent potential approximation (CPA) [46–49]. The EMTO-CPA package was used to perform the density functional theory calculations of the MPEA. The one-electron equations were solved using the scalar relativistic approximation and soft-core scheme. The Perdew-Burke-Ernzerhof generalized gradient approximation (PBE) [50] was used to approximate the exchange-correlation functional. The EMTO Green's function was calculated self-consistently for 16 exponentially distributed complex energy points [51]. Given the relatively low Curie temperature of CoNiCr, the magnetic states of the fcc CoNiCr-based alloys were assumed to be paramagnetic.

The total energy method [52–54], which is based on the excess total energy associated with the formation of a stacking fault in an ideal face-centered cubic lattice, was employed in the stacking fault energy calculations. The energy change associated with shifting a particular atomic layer in a certain direction to form a stacking fault indicates the energy preference of the stacking fault. Adjustments were made to the compositions of the slip planes surrounding the stacking fault, but the overall composition of the alloy was fixed. To eliminate the interaction between slip layers from the periodic lattice, it is generally necessary to build a multilayer supercell. During the generalized stacking fault energy (GSFE) calculation, a supercell model of 9 fcc (111) [55–57] planes was used. The stacking fault was simulated by applying a gliding Burgers vector $n\mathbf{b}_p$ ($\mathbf{b}_p = a_0\langle\bar{2}11\rangle/6$, a_0 is the lattice constant) parallel to the stacking fault direction. Based on the 9-layer model, the k-mesh was carefully tested for convergence and a 12×24×3 mesh was used for all calculations.

3. Results

3.1 Sample composition and as-annealed microstructure

The composition of the alloys investigated is listed in **Table 1**. A series of MPEAs with nominal composition of $Ni_{35}Co_{35}Cr_{(30-x)}Mo_x$ (x value in atomic ratio, x = 0, 5, and 10) were designed. Owing to the unique microstructural responses to stress with deformation twinning (DT) in NiCoCr-based alloys, a commercially pure Ni sample, and the alloys with different content of Mo, i.e., 0-Mo, 5-Mo, and 10-Mo were designated to be DT0, DT1, DT2, and DT3, respectively. **Fig. 1** shows the representative grain microstructure maps obtained by SEM-EBSD measurements for the DT alloys that were hot-rolled and annealed. The grain structures of the four DT alloys are composed of fully recrystallized single phase, and equiaxed grains that are mostly surrounded by high-angle grain boundaries. The fraction of annealing twin boundaries, specifically Σ3 type boundaries, was found to increase with Mo addition. The mean grain size (*d*), including annealing twin boundaries ranged from 80 μm to 19.6 μm and decreased with an elevated level of Mo addition. The reconstructed stereographic triangle (inverse pole figure (IPF)) was calculated by AztecCrystal analysis software. According to the IPF map, the frequency of occurrence of the crystal orientation parallel to the normal direction (ND), i.e., the maximum texture intensity (I_{max}) for the DT0 alloy, was slightly higher than the rest of the DT counterparts. Although slightly oriented <111> fibers along the ND are present, it should be noted that the I_{max} in these four DT alloys was low as no strong texture developed.

Table1. Nominal composition of pure Ni (DT0) and $Ni_{35}Co_{35}Cr_{30-x}Mo_x$ MPEAs (DT1, DT2, and DT3) in atomic ratio.

Alloys	Ni	Co	Cr	Mo	Fe	B
DT-0	100	-	-	-	-	-
DT-1	35.0	35.0	30.0	-	-	0.03
DT-2	35.0	35.0	25.0	5	-	0.03
DT-3	35.0	35.0	20.0	10	-	0.03

3.2 Mechanical properties of as-annealed DT alloys

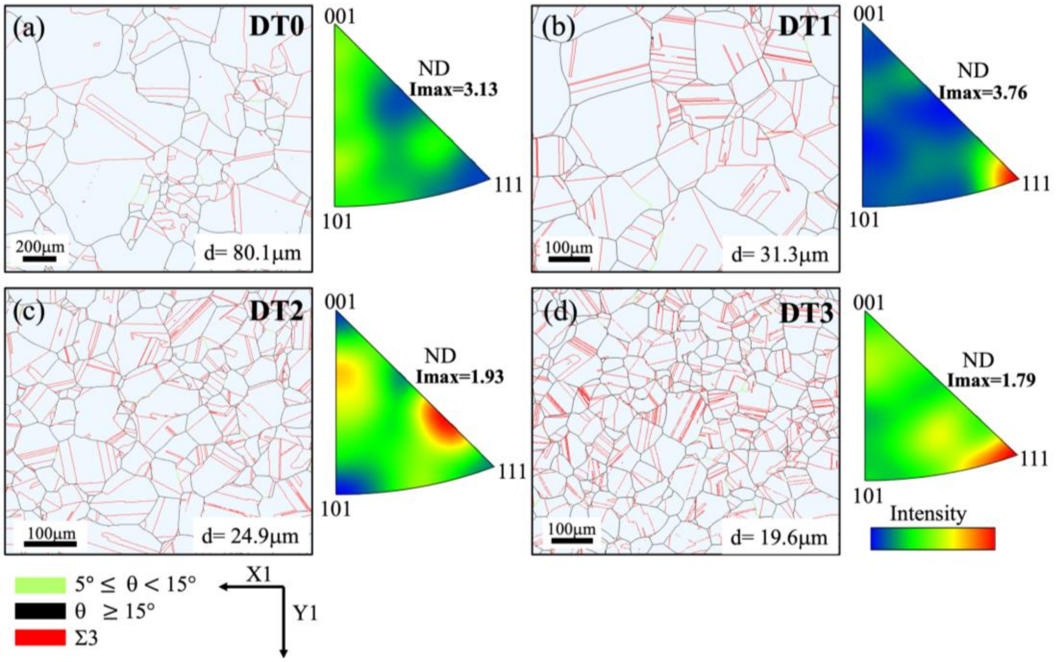

Fig. 1: EBSD grain boundary maps of fully recrystallized samples of (a) DT0, (b) DT1, (c) DT2, and (d) DT3. The green lines in the GB maps represent low angle boundaries with rotation angle (θ), 5° ≤ θ < 15°, black lines represent high angle boundaries with rotation angle (θ), θ≥15°, and red lines represent annealing twin boundaries (Σ3). Grain orientation distribution indicate that no strong texture was developed.

Fig. 2 presents the true stress-strain curves and strain hardening rate curves for as-annealed DT alloys. It is evident from the curves that the DT1 alloy demonstrates superior mechanical properties compared to pure Ni (DT0), with a higher yield strength of 204 MPa and a significantly larger fracture elongation of 82%. As Mo progressively replaces Cr in equal atomic percentages of 5% and 10% in DT2 and DT3, respectively, a discernible reduction in mean grain size was observed as depicted in **Fig. 1**. This Mo incorporation manifests in a substantial enhancement of both yield and ultimate tensile strength from 204/1490 MPa in Mo-free DT1 to 376/1750 MPa in Mo-added DT3. The plot in **Fig. 2(b)** showcases the strain-hardening rates for four distinct sample types as a function of true strains, illustrating that the strain-hardening behavior of DT1-3 differs significantly from that of DT0. A steady increase in strain hardening rate was observed in strains ranging from 0.1 to 0.5 for DT1-3, followed by an abrupt decline leading to failure. In contrast, DT0 showed a steady decrease in strain hardening rate throughout the entire deformation. To examine the effect of Mo on strain hardening, a series of loading-unloading-reloading (LUR) experiments was conducted on DT1 and 3, aiming to explore the evolution of back stress at varying strain levels. In **Fig. 2(c),** each LUR curve includes fourteen hysteresis cycles (corresponding to true strain of 0.05, 0.1, 0.15, 0.2, 0.25, 0.3, 0.35, 0.4, 0.45, 0.5, 0.55, 0.6, 0.65, 0.7). The Bauschinger effect (BE) is illustrated through the hysteresis loops (as depicted in **Fig. 2(c)-(d)**), revealing that reverse yielding occurs while the applied stress is still in tension during unloading. It is widely accepted that the BE primarily arises from local back stress generated by dislocation pile-ups encountering obstacles. Back stress can be calculated based on the characteristics of the hysteresis loops of the LUR curve [58]. **Fig. 2(e)** shows the continuous increase of back stress in both DT alloys. The back stress of DT1 is initially lower by 91 MPa than that of DT3 at true strain of 0.05. This back-stress difference gets progressively larger with the level of deformation. At 0.7 true strain (prior to necking), the back stress of DT3 is as high as ~1.2 GPa and ~300 MPa higher than that of DT1. The higher back stress in DT3 suggests that alloying with Mo amplifies the long-range stress caused by pileups of geometrically necessary dislocations (GNDs). These deformation patterns associated with strain hardening behavior were carefully examined using S/TEM in the following section to clarify the underlying strain hardening mechanism.

3.3 Deformation microstructure of as-annealed DT alloys

Fig. 3 demonstrates the tensile curves, strain hardening curves, and the microstructural changes. **Fig. 3(a)** shows distinct two-stage strain-hardening behavior for DT0. The strain-hardening rate experiences a sudden decline at strains below 0.05, followed by a gradual decrease beyond this point. The BF-TEM images in **Fig. 3(a_1, a_2)** demonstrate that the primary deformation microstructure for DT0, subjected to tensile interruption at a true strain of 0.26, is characterized to be equiaxed dislocation cells. Heterogeneous dislocations with different characters gliding on multiple slip systems were revealed. The tangled dislocations between wavy slips promote the formation of dislocation cells, which is consistent with observations reported for medium-to-high SFE metals [59]. On the other hand, for DT1-3, the strain hardening curves can be divided into four stages that were defined as A ($\varepsilon < 0.05$), B ($0.05 < \varepsilon < 0.12$), C ($0.12 < \varepsilon < 0.4$), and D ($\varepsilon > 0.4$). In stage A, strain hardening rate considerably declines, which is comparable to that seen in DT0. Subsequently, the strain hardening rate reaches a plateau in stage B for a short strain window, then followed by a steady increase in strain hardening rate in stage C. Dark field (DF)-TEM images

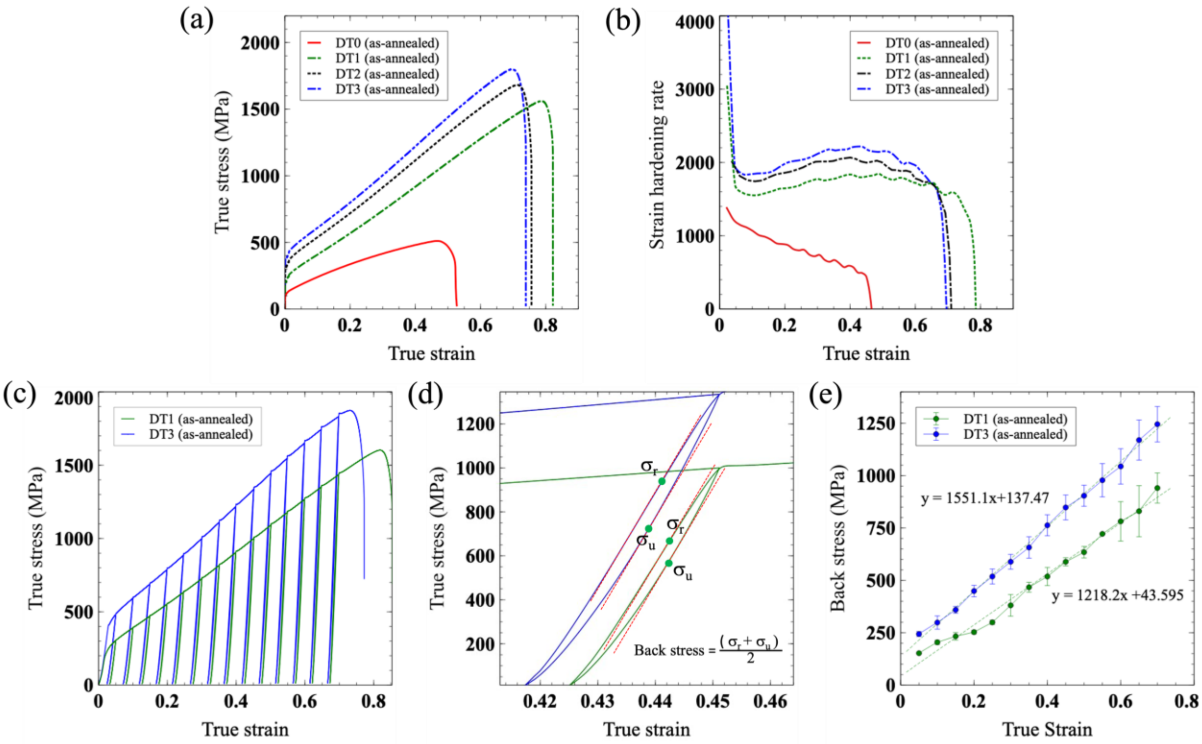

Fig. 2: (a) True stress-strain curves of as-annealed DT0, DT1, DT2, and DT3; (b) the strain hardening rate-true strain curves of as-annealed DT0, DT1, DT2, and DT3; (c) the loading-unloading-reloading curves of DT1 and DT3; (d) an enlarged region of (c) showing the reverse/reloading yield in a hysteresis loop; (e) the curves for the calculated back stress in DT1 and DT3.

shown in **Fig. 3 (b_1-b_2), (c_1-c_2), (d_1-d_2)** indicate that the main microstructural features after deformation are stacking faults and nano-twins. That is further supported by the associated diffraction patterns in **Fig. 3 (b_3, c_3, d_3)** where the streaks and extra diffraction spots correspond to the stacking faults and deformation twins oriented edge-on with respect to the electron beam direction. It should be noted that two unparallel faulting systems were activated and present with different morphologies, the one with the ribbon contrast was identified as SFs inclined to the beam direction while the other faulting system identified as a straight-line was oriented edge-on towards the zone axis of $<110>_{FCC}$. The remarkable enhancement in strain hardening observed in DT1-3 alloys may be attributed to the intersection of non-parallel stacking fault systems, as indicated by the yellow circles in **Fig. 3 (b_1, c_1, d_1)**. These intersections lead to the interaction of primary partial dislocations, further resulting in the formation of sessile stair-rod dislocations [60].

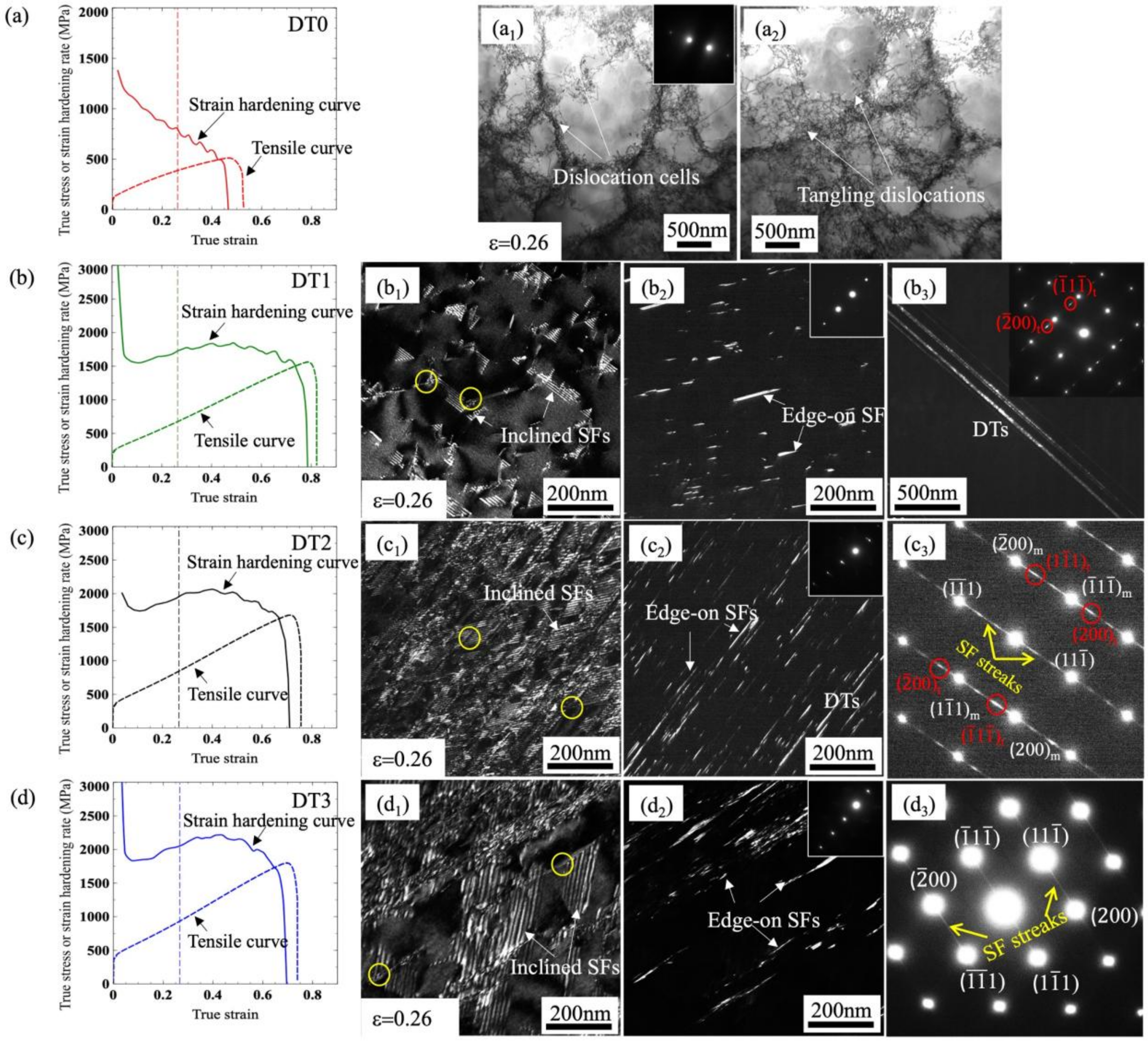

Fig. 3: (a-d) True stress-strain curves and strain-hardening curves of DT0-DT3, where the interrupted true strain (0.26) for purpose of TEM characterization is marked with dashed lines; (a_1-a_2) BF-TEM micrographs show the typical deformation microstructure with dislocation cells and tangling dislocations in DT0; (b_1-b_2) DF-TEM micrographs showing inclined and edge-on oriented SFs that slip on two conjugate slip systems in DT1; (b_3) representative deformation twins with a corresponding SAED pattern attached; (c_1-c_2) DF-TEM micrographs showing inclined, edge-on oriented SFs, and nano-twins that glide on two conjugate slip systems in DT2. (c_3) Corresponding SEAD pattern showing fine streaks (yellow arrows) and elongated extra spots (red circles), attributed to the shape factor of planar defects; (d_1-d_2) DF- TEM micrographs showing inclined, edge-on oriented SFs, and nano-twins that glide on two conjugate slip systems in DT3. (d_3) a corresponding SAED pattern showing fine streaks (yellow arrows), associated with the presence of SFs and nano-twins.

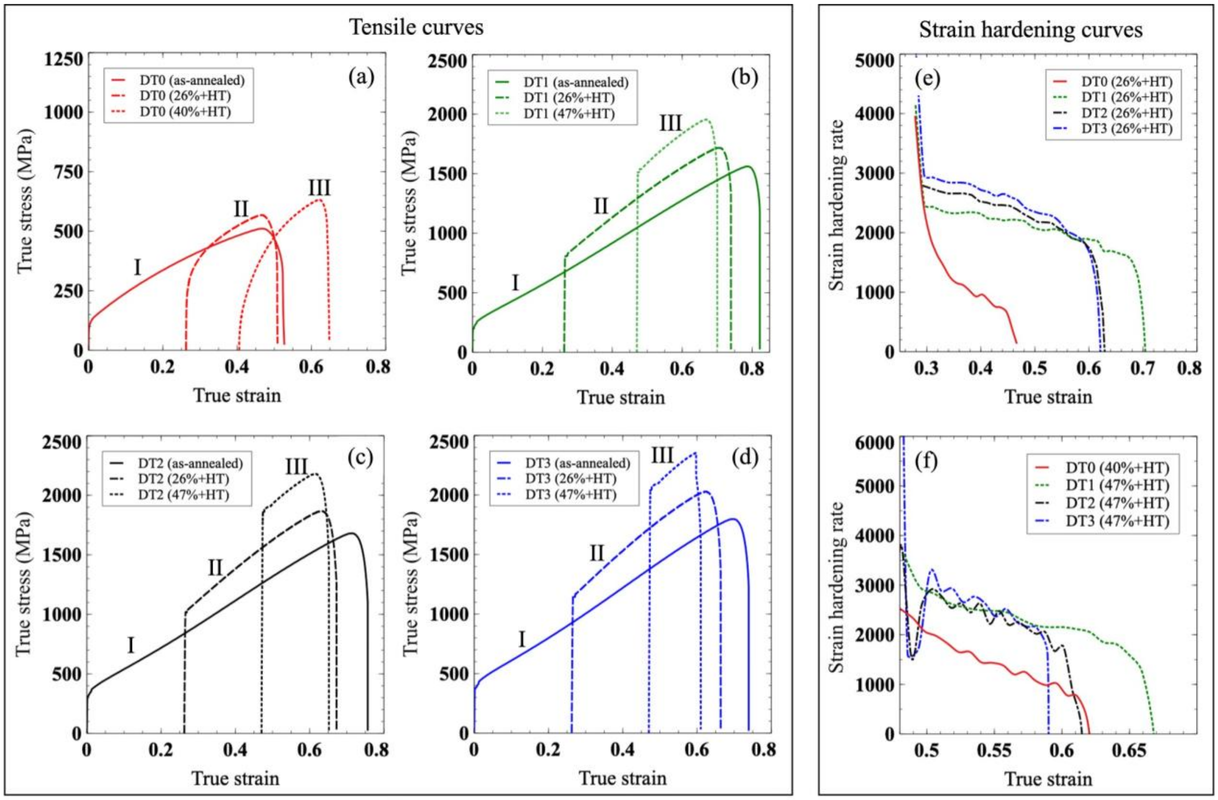

Fig. 4: True stress-strain curves of as-annealed DT alloys and pre-strained DT alloys with applied heat treatment. (a) DT0, (b) DT1, (c) DT2, and (d) DT3. Curves I correspond to the true stress-strain curves of as-annealed DT alloys. Curves II correspond to the true stress-strain curves of DT alloys that were pre-strained to 0.26 of true strain and aged. Curves III represent the true stress-strain curves for DT0 and DT1-3, which were pre-strained to 0.4 and 0.47 of true strain, respectively, and aged. (e-f) The strain hardening rate-true strain curves for DT0-3 that were pre-strained and aged; to true strain levels of 0.26 and 0.47.

3.4 Mechanical properties of pre-strained DT alloys post-heat treatment

In addition to strategies related to grain size refinement [20,61], solid solution strengthening [62,63], and SFE reduction [7,17,19] for mechanical strengthening, Suzuki hardening, i.e., strong chemical interaction between stacking faults (SFs) and specific elemental atoms [32,64,65], can lead to a significant increase in secondary hardening [33]. Based on this approach, the recrystallized DT alloys were subjected to uniaxial tensile deformation to two strain levels (true strain of 0.26 and 0.47), followed by a heat treatment and then reloaded for tensile testing. In **Fig. 4 (a-d),** the curves with solid lines are the stress-strain curves in uniaxial tensile loading of as-annealed DT0-3. The dashed curves in **Fig. 4 (a-d)** represent the stress-strain responses of samples that underwent initial tensile deformation, reaching a true strain of 0.26 (the curves are hence offset by that amount), followed by a heat treatment at 500°C for 1 hour and subsequent tensile reloading. This results in a softening effect for pure Ni (DT0) in **Fig. 4(a)**, while leading to a marked increased flow stresses in **Fig. 4(b-d)**, with steeper true stress-strain curves compared to the non-heat-treated samples. The dotted curves in **Fig. 4 (b-d)** exhibit the stress-strain responses of samples that were deformed in tensile loading to a true strain of 0.47 and heat-treated at 500°C for 1 hour. In such case, a pronounced increment in true stress was achieved up to 2.3 GPa in the 10-Mo added DT3 while maintaining a notable fracture elongation of 12%. After prior strain with heat treatment at 500°C for 1 hour, the stress-strain responses of DT0 differs from that of DT1-3 counterparts, with strain softening found in prior 0.26 and 0.4 true strains. To gain deeper insights into the plastic responses of heat-treated samples upon reloading, we constructed a plot in **Fig. 4(e, f)** to examine the strain hardening rate as a function of true strain. In **Fig. 4(e)**, it is evident that prior strains of 0.26, followed by heat treatment, significantly bolster the hardenability of DT1-3, whereas the strain hardening rate experiences an immediate reduction in DT0. Moving to **Fig. 4(f)** with 0.47 prior true strain, the resurgence of strain hardening rate in DT2 and DT3 delays the onset of necking. In **Fig. 5(a),** pre-strained DT1 and DT3 samples, followed by heat treatment at 500°C for 1 hour, were further tested using LUR experiment. The loading-unloading-reloading responses remain similar to the as-annealed, but with a higher true stress level due to the strengthening caused by the heat treatment. The back stress evolution as a function of true strain for DT1 and 3 is plot in **Fig. 5(b, c)**. The steeper slope of back-stress increment indicates that back-stress was intensified for DT alloys with heat treatment. The high back stress level implies the presence of effective BE caused by strong barriers to dislocation motion, which could be responsible for the high level of strain hardening rate shown in **Fig. 4(e, f)**.

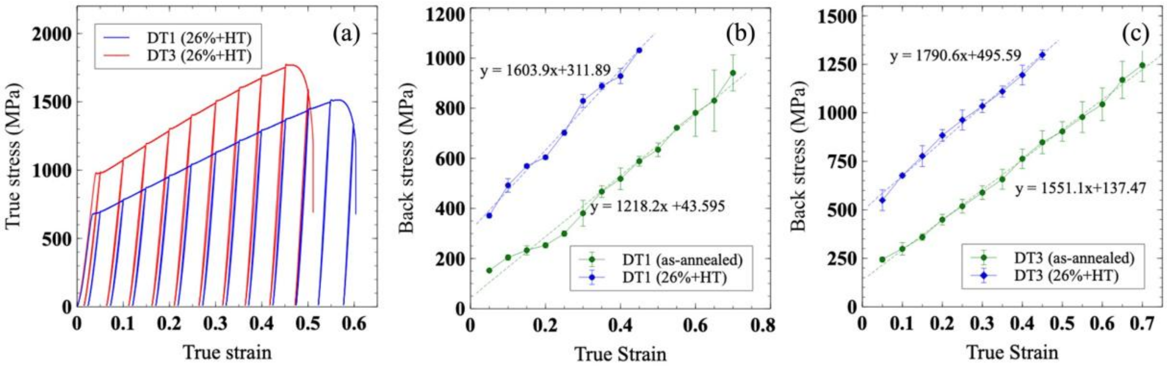

Fig. 5: (a) the LUR curves of pre-strained DT1 and DT3 with subsequent heat treatment, (b) the values of back stress as a function of true strain for as-annealed DT1 and pre-strained (0.26) DT1 with heat treatment, (c) the values of back stress as a function of true strain for as-annealed DT3 and pre-strained (0.26) DT3 with heat treatment.

3.5 Deformed microstructure of pre-strained DT alloys with heat treatment

SEM-EBSD and S/TEM analyses were carried out for samples that were pre-strained by true strain of 0.26 and heat-treated at 500°C for 1 hour. **Fig. 6** depicts the representative microstructure obtained by EBSD for DT0, 1, and 3. In all three samples, the IPF in **Fig. 6(a-c)** for crystal orientation along the tensile direction (TD) reveal a weak texture of <111>. Additionally, **Fig 6(g-i)** presents Kernel Average Misorientation (KAM) maps, which show a qualitative assessment of local misorientations influenced significantly by the density of geometrically necessary dislocations (GNDs). In **Fig. 6(g)**, certain grains within the DT0 sample exhibit minimal local misorientation, indicating the occurrence of partial recrystallization during heat treatment. This phenomenon provides a plausible explanation for the observed strain softening behavior depicted in **Fig. 4(a)**. Conversely, neither DT1 nor the DT3 alloys displayed recrystallization. The grain misorientation across the entire scanned region of DT1 and 3 remains high, underscoring that the heat treatment did not significantly annihilate GNDs. Although the deformation twinning behavior has been argued to be grain orientation dependent, i.e., the deformation twinning preferentially takes place in the <111> grains // TD, deformation twins in the present study have a thickness of only a few nanometers, and therefore they could not be resolved by the EBSD mapping.

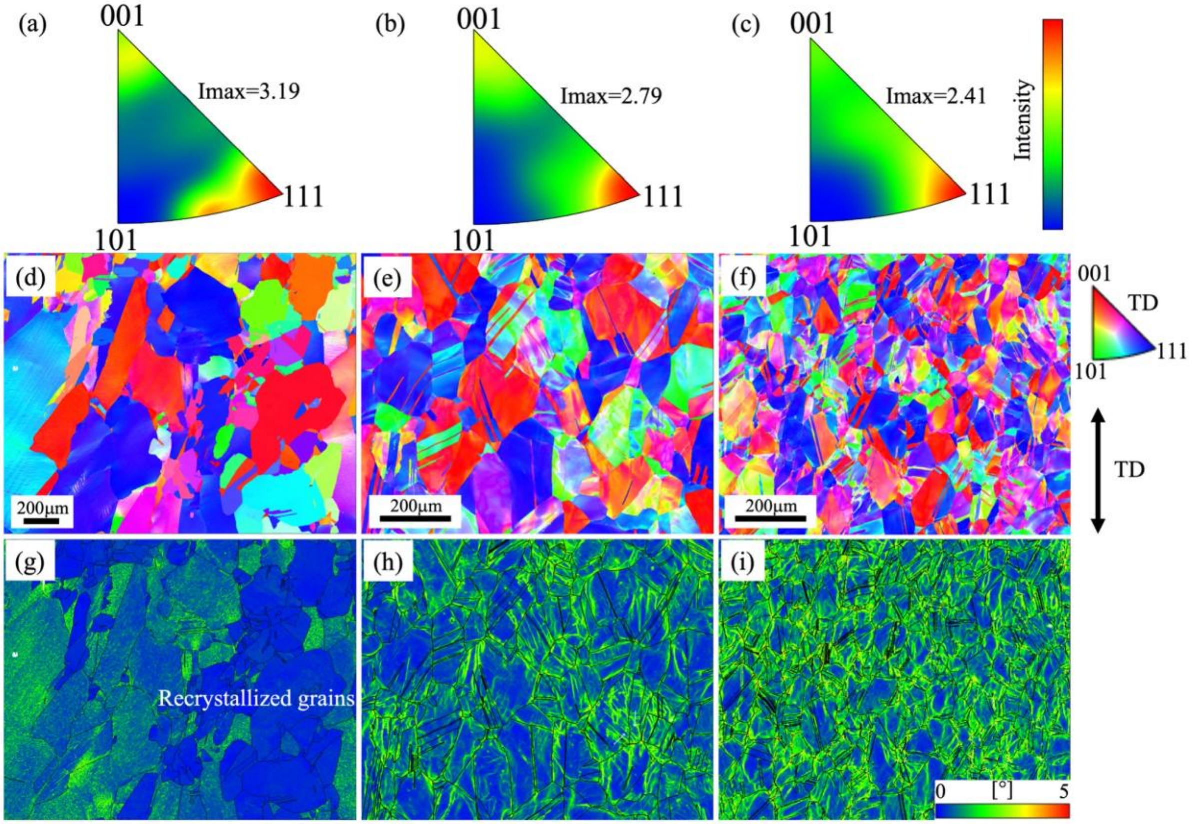

Fig. 6: EBSD maps of DT alloys pre-strained to a true strain of 0.26 and subsequently heat treated. (a-c) Grain orientation distributions indicate weak oriented <111> fiber texture along the tensile direction (TD) for DT0, DT1, and DT3; (d-f) Inverse pole figures of DT alloys; (g-i) The Kernel average misorientation (KAM) maps calculated by taking the points as well as all of its nearest neighbors into account with a criterion that the misorientation exceeding the threshold (5°) were disregarded.

The ADF-STEM DCI micrographs presented in **Fig. 7 (a, b, c)** illustrate the high-density of SFs and their mutual interactions/intersections. The heat treatment does not eliminate the pinned partial dislocations; in turn, **Fig. 7 (d, e, f)** shows that some unlocked SFs expand and terminate at intersection nodes (highlighted by yellow and red circles) wherever they encounter other SFs lying on conjugate slip planes. These intersection nodes circled in yellow are known for containing Lomer-Cotrell (L-C) locks with sessile dislocations acting as strong barriers to the motion of incoming dislocations, while intersection nodes circled in red are the dislocation network of extended nodes that can be ascribed to the reaction amongst glissile partials [66]. Despite no obvious microstructural changes during heat treatment, an elemental change does take place atomically as Cr segregation within multiple nano-sized fault planes was unveiled through a three-dimensional (3-D) reconstruction of atom probe tomography (APT) data for pre-strained and heat-treated DT2 in **Fig. 8(a)**. This was achieved by employing isoconcentration surfaces with a

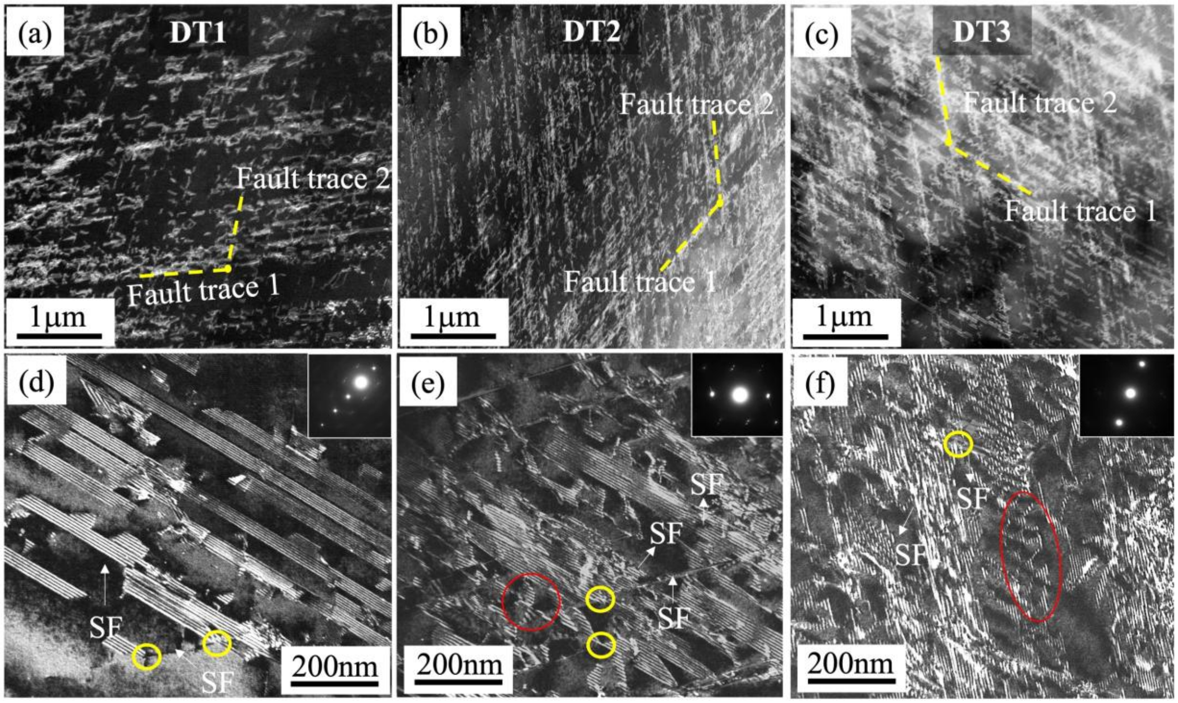

Fig. 7: The general deformation microstructure of pre-strained DT alloys with subsequent heat treatment. (a-c) The ADF-STEM DCI micrographs show enormous planar defect density on two conjugate slip systems; (b-f) The morphological details of unparallel stacking faults were revealed using DF-TEM. The intersections of SFs and the extended stacking-fault nodes were highlighted using yellow and red circles, respectively.

threshold of 62 at.% for the combined Ni and Co content. In **Fig. 8(a)**, the volume rendering with 4% Co, 4% Ni and 4% Cr is also used to highlight the segregation of elements at the fault and the proximity of it, distinguished from the solute segregation to crystallographic poles within the data. **Fig. 8(b)** showcases a one-dimensional concentration profile across fault planes, clearly demonstrating the preferential segregation of Cr to these planes at the expense of Co but minimal variation in Mo distribution. A slight Cr depletion was detected in close proximity to the right-hand side fault plane, indicating a localized diffusion phenomenon. Such fault segregation has been previously reported in greater detail for this family of NiCoCr-based alloys [64]. Interestingly, the Cr segregation width appears much thicker than what a structural fault plane would be, indicating that there is likely a gradient of Cr segregation across the fault plane as a result of the strain gradient – similar observations have been made for Cottrell atmospheres and grain boundaries in other alloys [67–69]. The Cr segregation is expected to increase the SF width and node size due to the reduction of SFE [70,71]. Indeed, **Figs. 8(c, d)** show the wide width and roughened landscape of nodes caused by Cr redistribution. Importantly, the heat-treatment induced segregation does not induce any local phase transformations within the SF planes, as evidenced by the representative high-resolution STEM micrographs in **Figs. 8 (e, f)**, which depict SFs with no discernible local phase transformations or precipitation decoration. Note that the Cr segregation revealed in the current study is consistent with some studies [36,64,72] but somewhat contradicts studies [35,73,74] showing Mo segregation. It should be emphasized that different characterization techniques may lead to different results. The interpretation of analytical STEM analysis for interface with chemical complexity [35,73,74] is complicated and greatly affected by sample thickness and the choice of the ionization edge [75]. The interface profile may differ by more than

1 nm which is too large to atomically resolve the chemistry variation within SFs. For this reason, the APT used in this work provides a better spatial resolution for elemental analysis. Additionally, alloy chemistry, processing and heat treatments that may promote other local phase equilibria and transformations may play a role in determining the structure and segregating atoms.

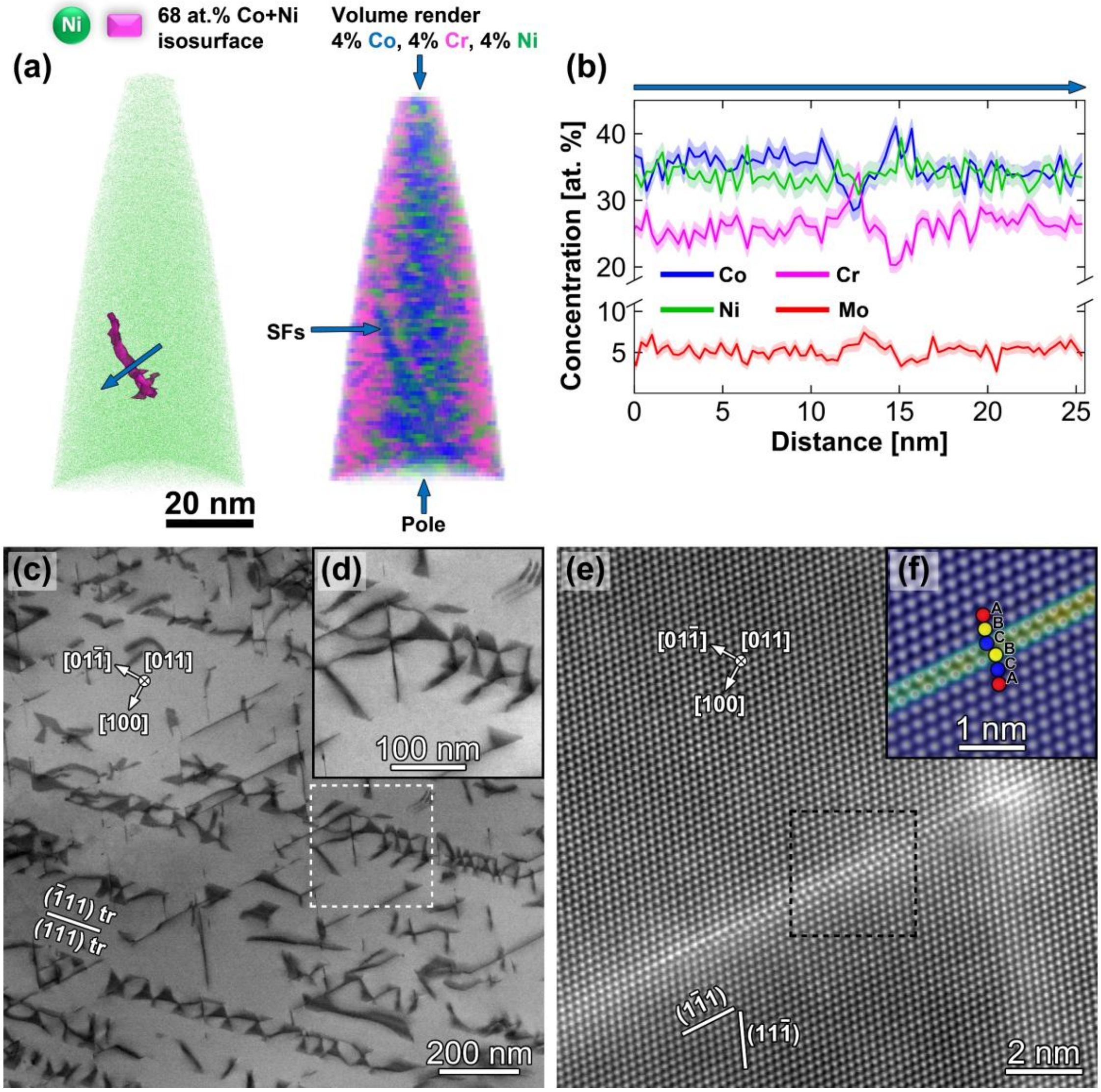

Fig. 8: (a) 3-D reconstruction of APT data in pre-strained and heat treated DT2 along with an overlay of a 62 at.% Cr + Ni isocomposition surface highlighting the Cr segregation in a nano-twin with multiple fault planes; (b) A 1-D concentration elemental profile across multiple fault planes; (c) BF-STEM DCI micrograph showing overview of the microstructure with many extended stacking-fault node configurations parallel with the active slip planes; (d) detail of extended stacking-fault nodes from the area highlighted by white dashed rectangle in (c). (e) Atomic resolution LAADF-STEM image of the intrinsic stacking fault parallel with $(1\bar{1}1)$ slip plane. (f) Detail from the area highlighted by black dashed rectangle in (e) shows Fast Fourier Transformation filtered HAADF-STEM overlapped with COS map further confirming ISF type of stacking sequence ABCBCA. Electron beam direction was parallel with [011] zone axis in (c-f).

5. Discussion

This study demonstrates a multi-length-scale approach to tailoring the mechanical properties of NiCoCr-based alloys through two distinct strengthening stages. In the first stage, the as-annealed sample was strengthened through Mo addition, which enhanced both Hall-Petch strengthening (via grain size reduction) and lattice distortion. In the second stage, additional strengthening was achieved through pre-straining followed by the third stage and the heat treatment, which promoted Suzuki segregation strengthening. The cumulative effects of alloying Mo content, prior strain, and heat treatment (HT) resulting in significant enhancement of yield stress while preserving good ductility are discussed.

5.1 The effect of Mo addition in as-annealed DT alloys

5.1.1 Grain size and lattice distortion

The Mo alloying effectively retards the grain growth during processing and recrystallization. With no secondary phases detected, the grain boundary strengthening, and solid solution hardening can contribute to a certain level of yield strength enhancement. Based on the well-known Hall Petch effect [76,77], the yield strength of polycrystalline materials can be described as:

$$\sigma_{YS} = \sigma_0 + kd^{-0.5} \qquad (1)$$

where σ_0 is the friction stress and solid-solution stress, k is the constant (Hall-Petch slope), and d is the mean grain size of the materials. Using values of σ_0 (218 MPa) and k (265 MPa·μm$^{0.5}$) determined for equiatomic CoCrNi by Yoshida et al. [78] reveals an estimated yield strength increase of 47.3 MPa is expected for DT1 and 59.8 MPa for DT3. This corresponds to an increase of 12 MPa for a grain size reduction of 11.7 μm. However, our tensile testing results revealed that alloying with 10 at.% of Mo increased the yield strength by 172.7 MPa, significantly exceeding this prediction. This suggests that Mo additions affect not only the grain size term ($kd^{-0.5}$) contributions via a reduction in grain size, but also significantly enhance the friction stress term (σ_0), which is strongly associated with the lattice distortion and solid solution hardening [12,78,79]. Based on this analysis, approximately 160 MPa of the strength increase from DT1 to DT3 can be attributed to lattice distortion and solid solution hardening induced by the 10 at.% Mo addition.

In contrast to conventional alloys, where solid solution strengthening effects dominate the σ_0 term due to interactions between the solute-dislocation stress fields, the local lattice distortion in a multi-component system results in an uneven energy landscape and a high energy barrier to the dislocation glide with unique hardening behavior [80]. CoCrNi-based alloys have shown a significantly higher lattice friction stress than pure Al and Ni metals, as certain elements in MPEAs have different atomic radii [78]. The levels of lattice distortion with different alloying elements have been assessed using mean square atomic displacement (MSAD) [12,13]:

$$\mathrm{MSAD} = \sum x_i \, (R_i - \bar{R})^2 \qquad (2)$$

where R_i and x_i are the nearest neighbor distance and the corresponding proportion, $\bar{R}$ is the mean nearest-neighbor distance of all element pairs [81]. The incorporation of Mo into CoCrNi-based alloys, leading to pronounced lattice distortion and enhanced mechanical properties, was recently investigated in a few prior studies. The findings of the current investigation are in agreement with the existing body of literature. With Mo alloying of the CoCrNi alloy, the critical role of a large refractory element, such as Mo, was found to lead to a higher value of MSAD and results in a higher yield strength when compared with the CoCrNi counterpart [13]. To explain the lattice distortion strengthening beyond conventional solid-solution strengthening models [82,83], Oh et al. [84,85] attempted to establish a linkage between the local lattice distortion and charge transfer among elements that affect the properties through atomic-level pressure and orbital transition. This approach was verified and applied to the $(CoNi)_{100-x}Mo_x$ system containing the refractory element Mo [37]. With increasing Mo content, charge transfer has been reported to introduce a higher atomic level pressure, implying a greater lattice distortion in alloys with a higher Mo content.

5.1.2 Stacking fault energy considerations

Many theoretical and experimental studies have been performed regarding the low SFEs in MPEAs [15,86,87]. Particularly, low to negative SFEs are frequently found in MPEAs. Despite being difficult to identify in experiments, negative SFEs do exist, as evidenced by the rich nano-twins and various close-packed nanostructures [88]. While the origin of this negative value of SFE is not well documented, it is generally believed to be related to the thermodynamic metastability of FCC's stacking sequence and the local atomic environment. The negative SFEs in FCC arrangements imply that the structural stability might be enhanced energetically by the local transformation of FCC to HCP stacking (formation of SFs on successive {111} planes) [89].

An extremely low SFE can lead to the transition of deformation features and the refinement of deformation twins. Wei et al. [15] suggest that the microscopic "deformation faulting" event could be caused by the effect of negative SFE, thus leading to a faulting plasticity via two paths: (1) the intersection between conjugate stacking faults with the formation of sessile dislocation; and (2) the elastic repulsion between parallel stacking faults. Given that similar deformation patterns (parallel/conjugate stacking fault interaction) were revealed in the TEM micrographs in **Fig. 3**, these two mechanisms [15], in addition to TWIP effect, appear to be responsible for the enhancement of strain hardening rate in the present as-annealed DT alloys. Regarding the elastic repulsion between parallel stacking faults, Pei et al. [86] proposed an alternative dislocation mechanism explaining the strengthening behavior. The enormous number of parallel partials dislocations may encounter one another and create new configurations as if they were in alloys with HCP lattice. As a result, the FCC structure works like dissociated basal dislocations on the basal plane in an HCP structure where the energy required for HCP partials motion is higher than that for FCC partials, indicating a higher critical resolved shear stress is required.

The first-principals calculation based on the compositions around DT1 and DT2 show a linear relationship with Cr/Co ratio in **Fig. 9**. A slight increase in Cr/Co ratio results in a linear SFE reduction from -23 to -36 (mJ/m^2) for CoCrNi and from -39 to -51 (mJ/m^2) for CoCrNi-Mo MPEAs. Furthermore, the Mo addition introduces complexity to the SFE landscape that universally reduces the SFE and enables facile SF expansion and intersection. When single isolated stacking faults on different slip planes collide and react, an assembled V-shaped stacking fault configuration with two Shockley partials bounding two edges and a stair-rod partial joining two conjugate ISFs can be created [60]. The V-shaped SFs configurations are frequently observed in **Figs. 3** and **7** and the most frequently reported stair-rod dislocations associated with V-shaped SF configuration in FCC metals and HEAs [90,91] are Lomer-Cotrell (L-C) locks (**b** = a/6 <110>) and Hirth locks (**b** = a/3 <001>). Qi et al.[92] suggest that L-C locks were frequently observed in acute-angle V-shaped configuration while obtuse-angle V-shaped SF configuration usually leads to Hirth locks.

Figs. 10 (a-b) show an example of obtuse-angle V-shaped SF configuration in the DT2. Two conjugate ISFs contacting at edge were observed to have width of 23.5 and 26.4 nm respectively.

Analysis of Burgers circuits were drawn in **Figs. 10 (d-f)** indicating that $\mathbf{b_{1p}}$ = a/12 $[\bar{2}1\bar{1}]$, $\mathbf{b_{2p}}$ = a/12 $[2\bar{1}1]$, $\mathbf{b_{3p}}$ = a/12$[21\bar{1}]$, $\mathbf{b_{4p}}$ = a/12$[\bar{2}\bar{1}1]$. The $\mathbf{b_{2p}}$ = a/12$[2\bar{1}1]$ and $\mathbf{b_{3p}}$ = a/12 $[21\bar{1}]$ associated with sessile dislocation in the projection plane equal to 1/2 Aγ and 1/2 Cδ, respectively, based on the tetrahedron in **Fig. 10(c)**. The complete Burgers vectors of the partials were deduced to be γD or γB for $\mathbf{b_{2p}}$ and δB or δD for $\mathbf{b_{3p}}$. While four possible combination for sessile dislocation at the ISFs intersection are expected, they are all associated with Hirth stair-rod dislocation with Burgers vector of a/3[001]:

I. $\gamma B + \delta B = a/6\,[233] = a/3[100]_{\text{Hirth stair-rod}} + a/2[011]_{\text{screw}}$

II. $\gamma B + \delta D = a/3\,[100]_{\text{Hirth stair-rod}}$

III. $\gamma D + \delta B = a/3\,[100]_{\text{Hirth stair-rod}}$

IV. $\gamma D + \delta D = a/6[2\bar{3}\bar{3}] = a/3[100]_{\text{Hirth stair-rod}} + a/2[0\bar{1}\bar{1}]_{\text{screw}}$

where the reactions would either lead to a single Hirth stair-rod dislocation or with a byproduct, pure screw perfect dislocation, along the direction perpendicular to the projection plane. As obtuse-angle and acute-angle V-shaped SF configurations are commonly observed in the present DT alloys with abundant SFs, it is likely that Hirth and L-C locks can act as critical obstacles to dislocation motion. Particularly, Mo-added DT2 and DT3 alloys with reduced SFE enable facile formation of Hirth and L-C locks that enhances strain hardening rate when compared to DT1 and postpone the occurrence of necking.

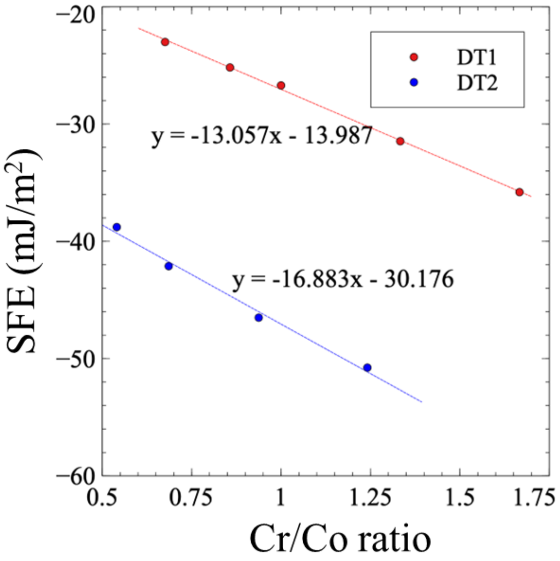

Fig. 9: First-principal calculations of SFE as a function of Cr/Co ratio. Mo-added DT2 exhibits universally lower SFE than Mo-free DT1.

5.2 The effect of Suzuki segregation in DT alloys

The lattice distortion and reduction of SFE caused by Mo addition have led to excellent mechanical properties. In addition, prior strain followed by a sub-recrystallization-temperature heat treatment extensively promotes a secondary hardening while maintaining an excellent ductility. The typical aged-hardened alloys are strengthened by the formation of precipitates from an oversaturated solid solution. However, neither nanosized precipitates nor HCP platelets were detected in the DT alloys in the SEM-EBSD phase maps or S/TEM micrographs, suggesting a precipitation hardening or TRIP is not responsible for this secondary hardening. **Fig. 11** graphically illustrates the substantial increments in strength ($\Delta\sigma_1$ and $\Delta\sigma_2$) across different levels of prior strains and the incorporation of Mo. Here, $\Delta\sigma_1$ represents the increase in strength at a given interrupted strain where the strengthening was achieved by subsequent heat treatment. $\Delta\sigma_2$ represents the increase in ultimate tensile strength. In **Fig 11 (b)**, the values of $\Delta\sigma_1$ and $\Delta\sigma_2$ shows a proportional increase in relation to prior strain level, i.e., the more SFs that formed during prior deformation, the higher the number of preferential Cr segregation sites for further strengthening. This rapid Cr transport mechanism taking place at the temperature of 500 °C is facilitated through a phenomenon known as "pipe diffusion" [93] via dislocations, which has been frequently reported [65,94]. Indeed, the APT data displayed in **Fig. 8 (a, b)** confirms the segregation of Cr within multiple fault planes at the cost of Co. The computation in **Fig. 9** verifies that the SFE can decrease with an increase of Cr/Co ratio and can be further reduced with the inclusion of Mo partitioning. This resulting undulated composition tuned by Cr segregation within the SF ribbon substantially varies the local SFE, presenting a roughened landscape that further affects the dislocation dynamics. Recent research indicates that the critical stress required to move a dislocation is directly related to the difference between unstable stacking fault energy (USFE) and stacking fault energy ($\Delta\gamma = \gamma_{usfe} - \gamma_{sfe}$) [95–97]. The spatial variation of $\Delta\gamma$ can be enhanced by undulated composition with Cr segregation that reduces the mobility of dislocations (curved dislocation motion). In addition, the complex energy landscape within and surrounding the SFs can potentially create more favorable conditions for interactions between Ni-Ni and Ni-Mo in the area. A molecular dynamic simulation performed by Jarlöv et al.[98] demonstrated that as the tendency of Cr–Co clustering reduced, the dislocation nucleation point can be shifted to the edges of the Ni–Ni clusters thus displaying a higher stress level of yielding. Ni-Mo interactions are believed to give rise to a short-range-ordered (SRO) microstructure, a characteristic phenomenon believed to strengthen Ni-Mo alloys [99,100]. However, whether the SRO microstructure indeed strongly affects the mechanical properties still remains under debate [101]. Multiple studies have suggested that the contribution of SRO may be significant for the initial dislocation gliding in a slip plane, but it is far less significant for the subsequent dislocation motion [102,103] or for highly deformed microstructures [75,76]. The observed increase in yield strength (400 MPa) induced by Cr segregation differs slightly from the 341 MPa increment reported for CoCrFeNiMo high entropy alloys [35] and the 250 MPa increase found in MP35N® [33]. This variation can be attributed to different processing methods: the CoCrFeNiMo high entropy alloys underwent cold rolling followed by heat treatment [35], while the MP35N® specimens were processed through wire drawing and aging [33].

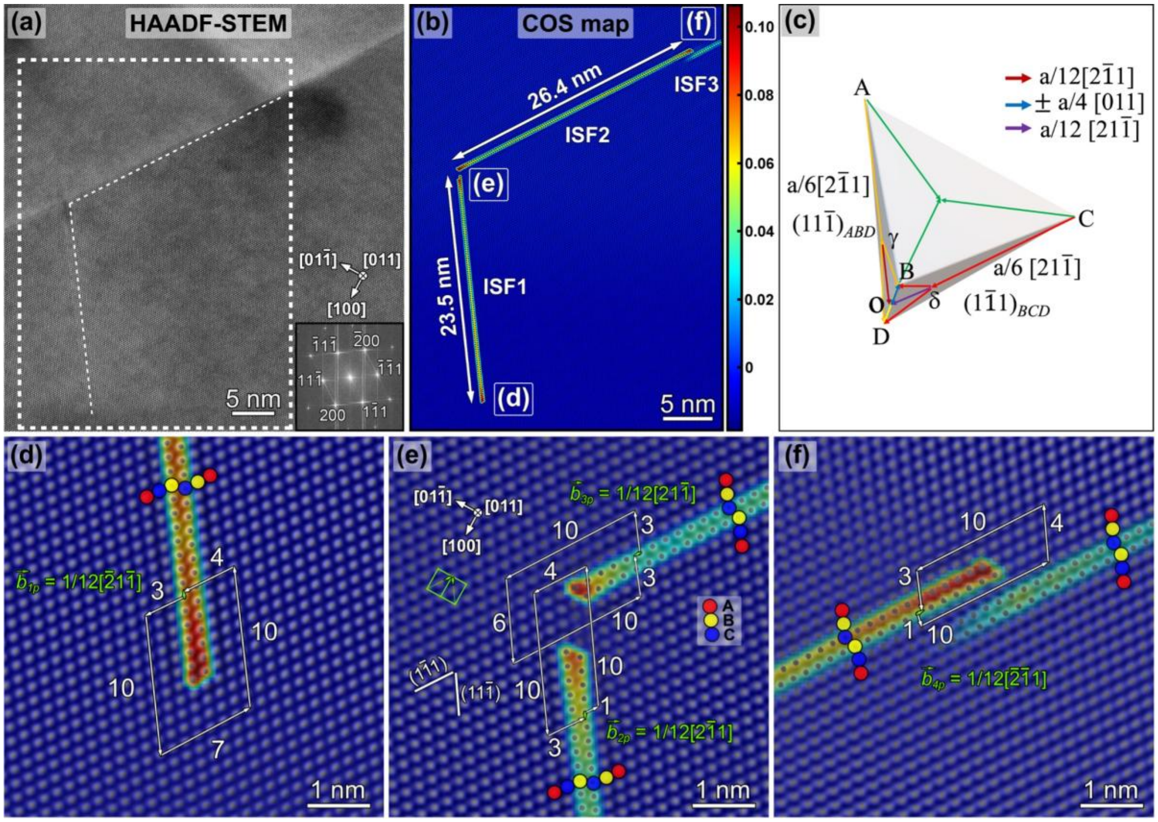

Fig. 10: (a) Atomic resolution HAADF-STEM image of V-shaped SF configuration with two Shockley partials bounding two edges and a stair-rod partial joining two conjugate ISFs; (b) Centre of symmetry (COS) analysis of the HAADF–STEM image; (c) the Thompson tetrahedron illustrating the Burgers vectors of dislocations involved in the SF interaction (d-f) higher magnification micrographs (COS maps overlapped with FFT filtered HAADF-STEM images) showing the partials' configuration and the analysis of the Burgers circuits. Electron beam is parallel to [011] zone axis.

Another perspective is that the decrease in SFE upon Mo partitioning would allow more stacking faults to form during pre-straining and serve as sites for Cr segregation. As a result, Cr segregation allows the stacking faults to expand from their unsegregated energy state and interact with other parallel / conjugate faulting systems. Afterwards, this heightened interaction among stacking faults revealed in **Fig. 10** will be extensively facilitated, i.e., the formation of sessile dislocations at SF intersection would increase the stress threshold required for dislocation motion. Finally, the increase in dislocation pile-ups due to dislocation locks would result in elevated levels of back-stress hardening, explaining the significant buildups of back stress for the sample with prior strain and heat treatment shown in **Fig. 5**.

5.3 Strengthening strategies comparison

Fig. 12 systematically illustrates the relationship between yield stress and Mo content across three distinct strengthening stages: (1) Hall-Petch strengthening and lattice distortion in as-annealed DT alloys (shown by the red curves), (2) strain hardening through the introduction of 30% and 60% prior engineering strains that promote TWIP effect and SF locks (illustrated by the blue curves), and (3) Suzuki segregation strengthening via subsequent heat treatment, which enhances alloys through further SF locks and interface hardening (represented by the green curves).

Using DT3 (10 at.% Mo) as an example, the initial yield strength reached 378 MPa in the as-annealed condition through grain refinement (Hall-Petch (H-P) strengthening) and lattice distortion. When annealed DT3 alloys was subjected to 60% prior engineering strain, the formation of extensive SFs and DTs strengthened the alloy through both SF intersection (L-C locks and Hirth locks) and the TWIP effects, increasing the yield strength to approximately 860 MPa. During subsequent heat treatment, these SFs served as Cr segregation sites for Suzuki hardening, ultimately elevating the yield strength to 1.26 GPa, demonstrating the cumulative effect of these strengthening mechanisms.

The wide-ranging mechanical properties of DT alloys, particularly in terms of yield strength and uniform elongation, are compared with those reported for single-phase HEAs, dual-phase (DP) HEAs, and TWIP steels in **Fig. 13**. The mechanisms for strengthening and strain hardening in the reported MPEAs can be summarized in the following: (1) CoNiV exhibits excellent yield strength of ~1 GPa due to the effect of severe lattice distortion caused by V [12], (2) TWIP steels show yield strength of ~800 MPa as strengthened by an ultrafine-grained microstructure [104], (3) $Co_{35}Cr_{25}Mn_{15}Ni_{15}Fe_{10}$ exhibits an exceptional ductility of 96% because of the effect of low SFE and TRIP effects [105], (4) CoCrNiW achieves enhanced ultimate tensile strength through tungsten additions, while maintaining excellent ductility due to its negative SFE. The negative SFE promotes stacking fault formation as the dominant deformation mechanism during plastic deformation, enabling effective macroscopic strain hardening [15]. By taking strategies (2) and (3), yield strength and ductility can be simultaneously improved by grain size refinement down to < 1 μm and by lowering SFE that sequentially activates different deformation modes (dislocation dynamics and deformation twinning) [104]. In the present study inspired by strategies mentioned above, the well-studied NiCoCr-based MPEAs, with their distinctive negative SFE and adjustable lattice distortion through refractory element additions, were utilized to showcase the wide range of mechanical properties achievable in this family of alloys. The strengthening associated with grain size refinement, severe lattice distortion, and SFE reduction can be achieved by alloying Mo that not only improves the yield strength but also maintain the excellent ductility. Due to their low-SFE characteristic, the SF density can be controlled by prior strain that intentionally creates numerous Cr segregation sites for tuning local SFE during 500°C heat treatment. As Cr segregation takes place, the SFE undulation (curved dislocation motion) and the complex SF intersection (L-C and Hirth locks) would impede the dislocation motion. Depending on the industrial applications, extremes of mechanical properties can be achieved without significant changes in material's chemistry [12][78][77]. **Table 2** shows that the engineering yield strength of the alloys can be tailored in a range from 204.0 to 1268.1 MPa with corresponding uniform elongation from 109% to 17%. This research proposes an alternate method to design alloys with mechanical properties customized for potential specific targeted applications. Many high-Cr concentration alloys with FCC structures, including commercial NiCoCr-based alloys HAYNES® HR-160® and MP35N®, are expected to benefit from the strengthening strategy associated with Cr segregation proposed here. Moreover, our work indeed suggests that this strategy can be expanded to other alloy families provided that they form extended faults during deformation, and that an element in the alloy tends to segregate to faults upon heat treatment.

Table. 2 Engineering yield strength (σ_{ys}), ultimate strength (σ_{uts}), uniform elongation (%), and fracture elongation for as-annealed DT alloys and pre-strained DT alloys with heat treatment.

Alloy	σ_{ys} (MPa)	σ_{uts} (MPa)	Uniform elongation (%)	Facture elongation (%)
DT1-annealed	204.0	718.3	109%	127%
DT2-annealed	310.8	832.0	94%	113%
DT3-annealed	378.7	906.3	93%	109%
DT1-0.3+HT	617.2	857.5	66%	79%
DT2-0.3+HT	780.5	1003.6	51%	66%
DT3-0.3+HT	876.5	1100.0	49%	64%
DT1-0.6+HT	941.7	1010.2	27%	41%
DT2-0.6+HT	1154.9	1190.2	17%	32%
DT3-0.6+HT	1268.1	1300.6	17%	23%

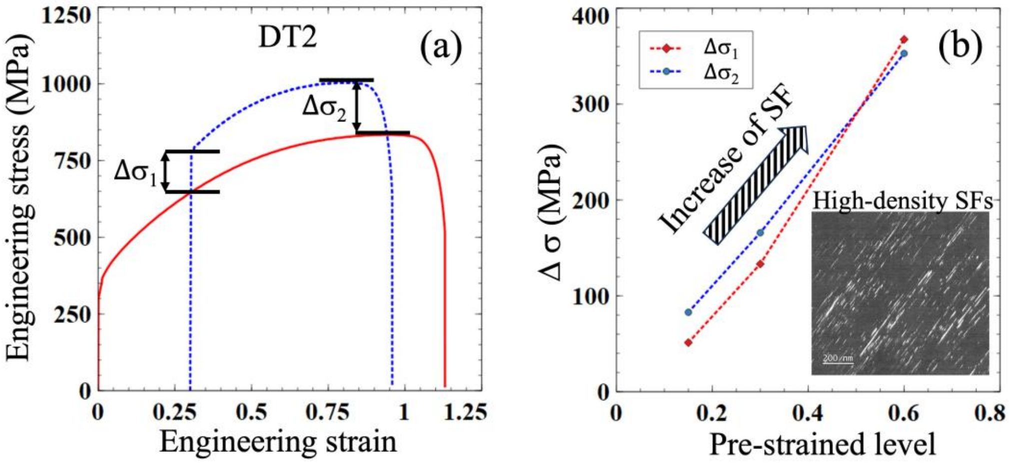

Fig. 11: (a) The engineering stress- strain curve depicting the measurement used to determine the increase of strength (σ_1 and σ_2) for the alloys that were pre-strained and aged; (b) The curve showing the increase of σ_1 and σ_2 as a function of pre-strain level (increase in SF amount in the microstructure).

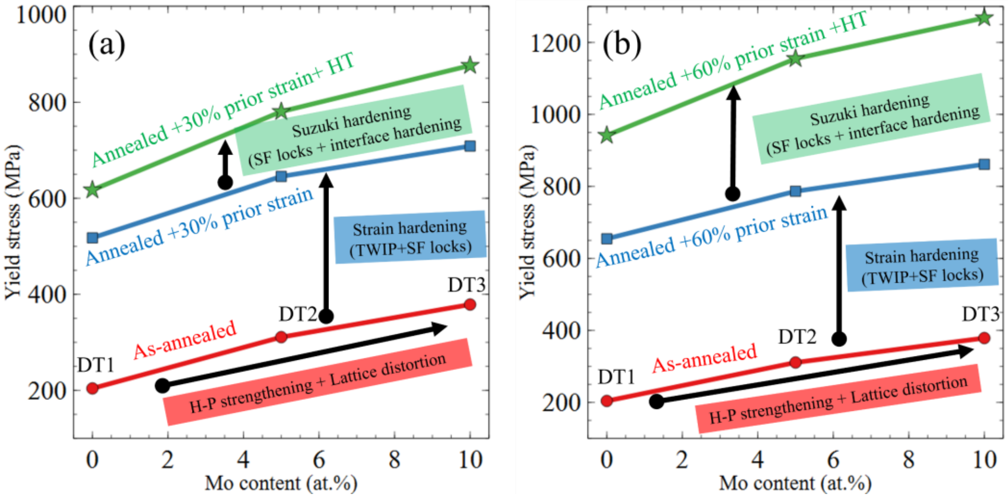

Fig. 12 The relationship between yield stress and Mo content demonstrates the cumulative effect of three strengthening mechanisms: (a) Comparison of yield stress achieved with 30% prior strain and (b) with 60% prior strain. Three distinct stages consisting of different sets of strengthening mechanisms are highlighted: Hall-Petch (H-P) strengthening and lattice distortion in the as-annealed state (red), strain hardening through TWIP effect and SF locks (blue), and Suzuki hardening with interface strengthening after heat treatment (green). The cumulative effects of higher Mo content, prior strain, and heat treatment (HT) result in significant yield stress enhancement, reaching maximum values of ~900 MPa and ~1260 MPa for 30% and 60% prior strain, respectively.

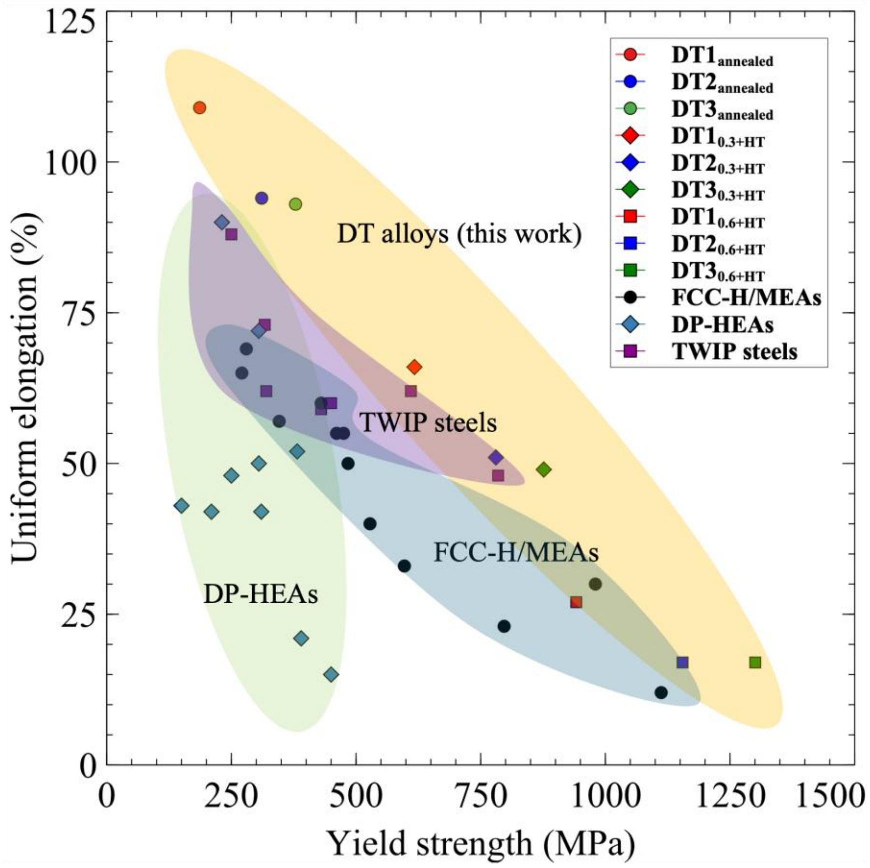

Fig.13: A comparison of mechanical properties of DT alloys with reported single-phase HEAs [1,2,12,13,15,30,106,107], DP-HEAs [105,108–112], and TWIP steels [104,113–115].

6. Conclusions

This study presents an alternative strategy for tailoring the mechanical properties of NiCoCr-based MPEAs through alloying with Mo and the implementation of Suzuki segregation phenomenon (Cr segregation). The systematic mechanical tests and the corresponding microstructural characterizations have drawn the following conclusions:

(1) Addition of Mo not only effectively retards the grain growth, but also strongly improves the mechanical properties. Addition of 10 at.% of Mo in DT3 improves the yield strength by 85% with only ~10% decrease in fracture elongation.

(2) The addition of Mo enhances the mechanical properties by (i) severe lattice distortion caused by the large atomic radius of Mo, (ii) retarding the grain growth leading to Hall-Patch strengthening, and (iii) SFE reduction that promotes complex SF interactions and intersections that frustrate the dislocation dynamics/mobility.

(3) The APT revealed that SFs serve as a preferential Cr segregation site at expense of Co during 500°C heat treatment. The SFE decreases with an increase of Cr/Co ratio and can be further reduced with the inclusion of Mo partitioning. This resulting undulated composition tuned by the Cr segregation associated with the SFs substantially varies the local SFE, presenting a roughened landscape and further retarding the dislocation dynamics/mobility. Moreover, a reduction of local SFE within SFs can potentially release the SFs from thermodynamic contraction, allowing them to interact with other parallel/conjugate faulting systems. The SFs interactions with V-shaped configurations generally comprised of L-C and Hirth locks what significantly enhances the strength and strain hardening rate.

(4) Depending on the potential targeted applications, extremes of mechanical properties can be achieved without significant changes in NiCoCr-based alloys´ chemistry. With careful control of Mo addition as well as prior strain level with subsequent heat treatment, the alternative strategy tailors the engineering yield strength of the alloys in a range from 204.0 to 1268.1 MPa with corresponding uniform elongation ranging from 109% to 17%. Since the significant role of Cr segregation in the alloy, the strengthening strategy can be expected to be tunable in the commercial alloys with high-Cr concentrations and the FCC structure.

Acknowledgements

This work was performed in support of the US Department of Energy’s Fossil Energy and Carbon Management Office’s Advanced Energy Materials Research Program and executed through the National Energy Technology Laboratory Research & Innovation Center (Advanced Energy Materials MYRP-1025034). The authors would like to thank C. McKaig and J. Willis for assistance in melting, R.E. Chinn and C. McKaig for chemistry analysis, and Christopher D. Powell for tensile tests. MJM and MH acknowledge financial support from the National Science Foundation under GOALI: / DMREF NSF #2323717. The multi-scale electron microscopy-based characterization was partially performed at the Center for Electron Microscopy and Analysis (CEMAS) at The Ohio State University. Atom probe tomography from PNNL was supported by the U.S. Department of Energy, Office of Science, Basic Energy Sciences, Materials Sciences and Engineering Division as a part of the Early Career Research program (FWP # 76052). The APT was conducted using facilities at Environmental Molecular Sciences Laboratory (EMSL), which is a DOE national user facility funded by Biological and Environmental Research Program located at Pacific Northwest National Laboratory. W.C. and C.L. acknowledges the support by the National Science Foundation under Grant No. 2415119.

Disclaimer

References

[1] G. Laplanche, A. Kostka, C. Reinhart, J. Hunfeld, G. Eggeler, E.P. George, Reasons for the superior mechanical properties of medium-entropy CrCoNi compared to high-entropy CrMnFeCoNi, Acta Mater 128 (2017) 292–303. https://doi.org/10.1016/j.actamat.2017.02.036.

[2] B. Gludovatz, A. Hohenwarter, K.V.S. Thurston, H. Bei, Z. Wu, E.P. George, R.O. Ritchie, Exceptional damage-tolerance of a medium-entropy alloy CrCoNi at cryogenic temperatures, Nat Commun 7 (2016) 10602. https://doi.org/10.1038/ncomms10602.

[3] J. Miao, C.E. Slone, T.M. Smith, C. Niu, H. Bei, M. Ghazisaeidi, G.M. Pharr, M.J. Mills, The evolution of the deformation substructure in a Ni-Co-Cr equiatomic solid solution alloy, Acta Mater 132 (2017) 35–48. https://doi.org/https://doi.org/10.1016/j.actamat.2017.04.033.

[4] A. Gali, E.P. George, Tensile properties of high- and medium-entropy alloys, Intermetallics (Barking) 39 (2013) 74–78. https://doi.org/https://doi.org/10.1016/j.intermet.2013.03.018.

[5] B. Gludovatz, A. Hohenwarter, D. Catoor, E.H. Chang, E.P. George, R.O. Ritchie, A fracture-resistant high-entropy alloy for cryogenic applications, Science 345 (2014) 1153–1158. https://doi.org/10.1126/science.1254581.

[6] G. Laplanche, A. Kostka, O.M. Horst, G. Eggeler, E.P. George, Microstructure evolution and critical stress for twinning in the CrMnFeCoNi high-entropy alloy, Acta Mater 118 (2016) 152–163. https://doi.org/https://doi.org/10.1016/j.actamat.2016.07.038.

[7] D.T. Pierce, J.A. Jiménez, J. Bentley, D. Raabe, J.E. Wittig, The influence of stacking fault energy on the microstructural and strain-hardening evolution of Fe–Mn–Al–Si steels during tensile deformation, Acta Mater 100 (2015) 178–190. https://doi.org/10.1016/j.actamat.2015.08.030.

[8] I. Gutierrez-Urrutia, D. Raabe, Dislocation and twin substructure evolution during strain hardening of an Fe–22 wt.% Mn–0.6 wt.% C TWIP steel observed by electron channeling contrast imaging, Acta Mater 59 (2011) 6449–6462. https://doi.org/10.1016/J.ACTAMAT.2011.07.009.

[9] H. Chang, T.W. Zhang, S.G. Ma, D. Zhao, R.L. Xiong, T. Wang, Z.Q. Li, Z.H. Wang, Novel Si-added CrCoNi medium entropy alloys achieving the breakthrough of strength-ductility trade-off, Mater Des 197 (2021) 109202. https://doi.org/10.1016/j.matdes.2020.109202.

[10] T.T. Huang, W.J. Dan, W.G. Zhang, Study on the Strain Hardening Behaviors of TWIP/TRIP Steels, Metallurgical and Materials Transactions A 48 (2017) 4553–4564. https://doi.org/10.1007/s11661-017-4245-0.

[11] S. Chen, H.S. Oh, B. Gludovatz, S.J. Kim, E.S. Park, Z. Zhang, R.O. Ritchie, Q. Yu, Real-time observations of TRIP-induced ultrahigh strain hardening in a dual-phase CrMnFeCoNi high-entropy alloy, Nat Commun 11 (2020) 826. https://doi.org/10.1038/s41467-020-14641-1.

[12] S.S. Sohn, A. Kwiatkowski da Silva, Y. Ikeda, F. Körmann, W. Lu, W.S. Choi, B. Gault, D. Ponge, J. Neugebauer, D. Raabe, Ultrastrong Medium-Entropy Single-Phase Alloys Designed via Severe Lattice Distortion, Advanced Materials 31 (2019) 1807142. https://doi.org/10.1002/adma.201807142.

[13] R. Chang, W. Fang, J. Yan, H. Yu, X. Bai, J. Li, S. Wang, S. Zheng, F. Yin, Microstructure and mechanical properties of CoCrNi-Mo medium entropy alloys: Experiments and first-principle calculations, J Mater Sci Technol 62 (2021) 25–33. https://doi.org/10.1016/j.jmst.2020.04.062.

[14] C.E. Slone, S. Chakraborty, J. Miao, E.P. George, M.J. Mills, S.R. Niezgoda, Influence of deformation induced nanoscale twinning and FCC-HCP transformation on hardening and texture development in medium-entropy CrCoNi alloy, Acta Mater 158 (2018) 38–52. https://doi.org/10.1016/j.actamat.2018.07.028.

[15] S. Wei, C.C. Tasan, Deformation faulting in a metastable CoCrNiW complex concentrated alloy: A case of negative intrinsic stacking fault energy?, Acta Mater 200 (2020) 992–1007. https://doi.org/10.1016/j.actamat.2020.09.056.

[16] C.-Y. Hung, Y. Bai, T. Shimokawa, N. Tsuji, M. Murayama, A correlation between grain boundary character and deformation twin nucleation mechanism in coarse-grained high-Mn austenitic steel, Sci Rep 11 (2021) 8468. https://doi.org/10.1038/s41598-021-87811-w.

[17] Y.Z. Tian, L.J. Zhao, S. Chen, A. Shibata, Z.F. Zhang, N. Tsuji, Significant contribution of stacking faults to the strain hardening behavior of Cu-15%Al alloy with different grain sizes, Sci Rep 5 (2015) 16707. https://doi.org/10.1038/srep16707.

[18] C. Niu, C.R. LaRosa, J. Miao, M.J. Mills, M. Ghazisaeidi, Magnetically-driven phase transformation strengthening in high entropy alloys, Nat Commun 9 (2018) 1363. https://doi.org/10.1038/s41467-018-03846-0.

[19] B.C. De Cooman, Y. Estrin, S.K. Kim, Twinning-induced plasticity (TWIP) steels, Acta Mater 142 (2018) 283–362. https://doi.org/10.1016/j.actamat.2017.06.046.

[20] C.-Y. Hung, Y. Bai, N. Tsuji, M. Murayama, Grain size altering yielding mechanisms in ultrafine grained high-Mn austenitic steel: advanced TEM investigations, J Mater Sci Technol 86 (2021) 192–203. https://doi.org/10.1016/j.jmst.2021.01.031.

[21] C.-Y. Hung, T. Shimokawa, Y. Bai, N. Tsuji, M. Murayama, Investigating the dislocation reactions on Σ3\{111\} twin boundary during deformation twin nucleation process in an ultrafine-grained high-manganese steel, Sci Rep 11 (2021) 19298. https://doi.org/10.1038/s41598-021-98875-z.

[22] P. Sathiyamoorthi, P. Asghari-Rad, J.W. Bae, H.S. Kim, Fine tuning of tensile properties in CrCoNi medium entropy alloy through cold rolling and annealing, Intermetallics 113 (2019) 106578. https://doi.org/10.1016/j.intermet.2019.106578.

[23] P. Sathiyamoorthi, J. Moon, J.W. Bae, P. Asghari-Rad, H.S. Kim, Superior cryogenic tensile properties of ultrafine-grained CoCrNi medium-entropy alloy produced by high-pressure torsion and annealing, Scr Mater 163 (2019) 152–156. https://doi.org/10.1016/j.scriptamat.2019.01.016.

[24] F. Otto, A. Dlouhý, Ch. Somsen, H. Bei, G. Eggeler, E.P. George, The influences of temperature and microstructure on the tensile properties of a CoCrFeMnNi high-entropy alloy, Acta Mater 61 (2013) 5743–5755. https://doi.org/10.1016/j.actamat.2013.06.018.

[25] T. Yang, Y.L. Zhao, Y. Tong, Z.B. Jiao, J. Wei, J.X. Cai, X.D. Han, D. Chen, A. Hu, J.J. Kai, K. Lu, Y. Liu, C.T. Liu, Multicomponent intermetallic nanoparticles and superb mechanical behaviors of complex alloys, Science 362 (2018) 933–937. https://doi.org/10.1126/science.aas8815.

[26] J.Y. He, H. Wang, H.L. Huang, X.D. Xu, M.W. Chen, Y. Wu, X.J. Liu, T.G. Nieh, K. An, Z.P. Lu, A precipitation-hardened high-entropy alloy with outstanding tensile properties, Acta Mater 102 (2016) 187–196. https://doi.org/10.1016/j.actamat.2015.08.076.

[27] Z.G. Wang, W. Zhou, L.M. Fu, J.F. Wang, R.C. Luo, X.C. Han, B. Chen, X.D. Wang, Effect of coherent L12 nanoprecipitates on the tensile behavior of a fcc-based high-entropy alloy, Materials Science and Engineering: A 696 (2017) 503–510. https://doi.org/10.1016/j.msea.2017.04.111.

[28] Y.L. Zhao, T. Yang, Y. Tong, J. Wang, J.H. Luan, Z.B. Jiao, D. Chen, Y. Yang, A. Hu, C.T. Liu, J.-J. Kai, Heterogeneous precipitation behavior and stacking-fault-mediated deformation in a CoCrNi-based medium-entropy alloy, Acta Mater 138 (2017) 72–82. https://doi.org/10.1016/j.actamat.2017.07.029.

[29] R. Chang, W. Fang, H. Yu, X. Bai, X. Zhang, B. Liu, F. Yin, Heterogeneous banded precipitation of (CoCrNi)93Mo7 medium entropy alloys towards strength–ductility synergy utilizing compositional inhomogeneity, Scr Mater 172 (2019) 144–148. https://doi.org/10.1016/j.scriptamat.2019.07.026.

[30] C.E. Slone, J. Miao, E.P. George, M.J. Mills, Achieving ultra-high strength and ductility in equiatomic CrCoNi with partially recrystallized microstructures, Acta Mater 165 (2019) 496–507. https://doi.org/10.1016/j.actamat.2018.12.015.

[31] N. Tsuji, S. Ogata, H. Inui, I. Tanaka, K. Kishida, S. Gao, W. Mao, Y. Bai, R. Zheng, J.-P. Du, Strategy for managing both high strength and large ductility in structural materials–sequential nucleation of different deformation modes based on a concept of plaston, Scr Mater 181 (2020) 35–42. https://doi.org/10.1016/j.scriptamat.2020.02.001.

[32] Y. Koizumi, T. Nukaya, S. Suzuki, S. Kurosu, Y. Li, H. Matsumoto, K. Sato, Y. Tanaka, A. Chiba, Suzuki segregation in Co–Ni-based superalloy at 973 K: An experimental and computational study by phase-field simulation, Acta Mater 60 (2012) 2901–2915. https://doi.org/10.1016/j.actamat.2012.01.054.

[33] D. Sorensen, B.Q. Li, W.W. Gerberich, K.A. Mkhoyan, Investigation of secondary hardening in Co–35Ni–20Cr–10Mo alloy using analytical scanning transmission electron microscopy, Acta Mater 63 (2014) 63–72. https://doi.org/10.1016/j.actamat.2013.10.005.

[34] Y.J. Xu, D.Q. Qi, K. Du, C.Y. Cui, H.Q. Ye, Stacking fault effects on dynamic strain aging in a Ni–Co-based superalloy, Scr Mater 87 (2014) 37–40. https://doi.org/10.1016/j.scriptamat.2014.05.012.

[35] J. Li, K. Yamanaka, Y. Hayasaka, A. Chiba, Suzuki hardening and segregation in Co0.95Cr0.8Fe0.25Ni1.8Mo0.475 high-entropy alloys, Scr Mater 226 (2023) 115260. https://doi.org/10.1016/j.scriptamat.2022.115260.

[36] H. Suzuki, Segregation of Solute Atoms to Stacking Faults, J Physical Soc Japan 17 (1962) 322–325. https://doi.org/10.1143/JPSJ.17.322.

[37] T.J. Jang, Y.N. Lee, Y. Ikeda, F. Körmann, J.-H. Baek, H.-S. Do, Y.T. Choi, H. Gwon, J.-Y. Suh, H.S. Kim, B.-J. Lee, A. Zargaran, S.S. Sohn, Compositive role of refractory element Mo in improving strength and ductility of face-centered-cubic complex concentrated alloys, Acta Mater 255 (2023) 119030. https://doi.org/10.1016/j.actamat.2023.119030.

[38] B. Cai, B. Liu, S. Kabra, Y. Wang, K. Yan, P.D. Lee, Y. Liu, Deformation mechanisms of Mo alloyed FeCoCrNi high entropy alloy: In situ neutron diffraction, Acta Mater 127 (2017) 471–480. https://doi.org/10.1016/j.actamat.2017.01.034.

[39] P.J. Phillips, M.C. Brandes, M.J. Mills, M. De Graef, Diffraction contrast STEM of dislocations: Imaging and simulations, Ultramicroscopy 111 (2011) 1483–1487. https://doi.org/10.1016/j.ultramic.2011.07.001.

[40] M. Heczko, V. Mazánová, R. Gröger, T. Záležák, M.S. Hooshmand, E.P. George, M.J. Mills, A. Dlouhý, Elemental segregation to lattice defects in the CrMnFeCoNi high-entropy alloy during high temperature exposures, Acta Mater 208 (2021) 116719. https://doi.org/10.1016/j.actamat.2021.116719.

[41] P. Pandey, M. Heczko, N. Khatavkar, N. Mazumder, A. Sharma, A. Singh, M.J. Mills, K. Chattopadhyay, On the faulting and twinning mediated strengthening and plasticity in a γ′ strengthened CoNi-based superalloy at room temperature, Acta Mater 252 (2023) 118928. https://doi.org/10.1016/j.actamat.2023.118928.

[42] L. Vitos, I.A. Abrikosov, B. Johansson, Anisotropic Lattice Distortions in Random Alloys from First-Principles Theory, Phys Rev Lett 87 (2001) 156401. https://doi.org/10.1103/PhysRevLett.87.156401.

[43] L. Vitos, B. Johansson, J. Kollár, H.L. Skriver, Exchange energy in the local Airy gas approximation, Phys Rev B 62 (2000) 10046–10050. https://doi.org/10.1103/PhysRevB.62.10046.

[44] L. Vitos, Total-energy method based on the exact muffin-tin orbitals theory, Phys Rev B 64 (2001) 014107. https://doi.org/10.1103/PhysRevB.64.014107.

[45] L. Vitos, Computational quantum mechanics for materials engineers: the EMTO method and applications, 2007. https://doi.org/10.1103/PhysRevB.62.10046.

[46] P. Soven, Coherent-Potential Model of Substitutional Disordered Alloys, Physical Review 156 (1967) 809–813. https://doi.org/10.1103/PhysRev.156.809.

[47] D.W. Taylor, Vibrational Properties of Imperfect Crystals with Large Defect Concentrations, Physical Review 156 (1967) 1017–1029. https://doi.org/10.1103/PhysRev.156.1017.

[48] B.L. Gyorffy, Coherent-Potential Approximation for a Nonoverlapping-Muffin-Tin-Potential Model of Random Substitutional Alloys, Phys Rev B 5 (1972) 2382–2384. https://doi.org/10.1103/PhysRevB.5.2382.

[49] J.P. Perdew, K. Burke, M. Ernzerhof, Generalized Gradient Approximation Made Simple, Phys Rev Lett 77 (1996) 3865–3868. https://doi.org/10.1103/PhysRevLett.77.3865.

[50] W. Li, S. Lu, Q.-M. Hu, S.K. Kwon, B. Johansson, L. Vitos, Generalized stacking fault energies of alloys, Journal of Physics: Condensed Matter 26 (2014) 265005. https://doi.org/10.1088/0953-8984/26/26/265005.

[51] H. Huang, X. Li, Z. Dong, W. Li, S. Huang, D. Meng, X. Lai, T. Liu, S. Zhu, L. Vitos, Critical stress for twinning nucleation in CrCoNi-based medium and high entropy alloys, Acta Mater 149 (2018) 388–396. https://doi.org/10.1016/j.actamat.2018.02.037.

[52] S. Kibey, J.B. Liu, D.D. Johnson, H. Sehitoglu, Predicting twinning stress in fcc metals: Linking twin-energy pathways to twin nucleation, Acta Mater 55 (2007) 6843–6851. https://doi.org/10.1016/j.actamat.2007.08.042.

[53] W. Zhao, W. Li, Z. Sun, S. Gong, L. Vitos, Tuning the plasticity of Ni-Mo solid solution in Ni-based superalloys by ab initio calculations, Mater Des 124 (2017) 100–107. https://doi.org/10.1016/j.matdes.2017.03.057.

[54] L.-Y. Tian, R. Lizárraga, H. Larsson, E. Holmström, L. Vitos, A first principles study of the stacking fault energies for fcc Co-based binary alloys, Acta Mater 136 (2017) 215–223. https://doi.org/10.1016/j.actamat.2017.07.010.

[55] X. Wang, R.R. De Vecchis, C. Li, H. Zhang, X. Hu, S. Sridar, Y. Wang, W. Chen, W. Xiong, Design metastability in high-entropy alloys by tailoring unstable fault energies, Sci Adv 8 (2022). https://doi.org/10.1126/sciadv.abo7333.

[56] J. Ren, M. Wu, C. Li, S. Guan, J. Dong, J.-B. Forien, T. Li, K.S. Shanks, D. Yu, Y. Chen, K. An, K.Y. Xie, W. Chen, T. Voisin, W. Chen, Deformation mechanisms in an additively manufactured dual-phase eutectic high-entropy alloy, Acta Mater 257 (2023) 119179. https://doi.org/10.1016/j.actamat.2023.119179.

[57] Y. Liu, J. Ren, S. Guan, C. Li, Y. Zhang, S. Muskeri, Z. Liu, D. Yu, Y. Chen, K. An, Y. Cao, W. Liu, Y. Zhu, W. Chen, S. Mukherjee, T. Zhu, W. Chen, Microstructure and mechanical behavior of additively manufactured CoCrFeMnNi high-entropy alloys: Laser directed energy deposition versus powder bed fusion, Acta Mater 250 (2023) 118884. https://doi.org/10.1016/j.actamat.2023.118884.

[58] M. Yang, Y. Pan, F. Yuan, Y. Zhu, X. Wu, Back stress strengthening and strain hardening in gradient structure, Mater Res Lett 4 (2016) 145–151. https://doi.org/10.1080/21663831.2016.1153004.

[59] P. Landau, R.Z. Shneck, G. Makov, A. Venkert, Evolution of dislocation patterns in fcc metals, IOP Conf Ser Mater Sci Eng 3 (2009) 012004. https://doi.org/10.1088/1757-899X/3/1/012004.

[60] J.P. Hirth, J. Lothe, T. Mura, Theory of Dislocations (2nd ed.), Krieger Publishing Company, 1983. https://doi.org/10.1115/1.3167075.

[61] W.Z. Han, Z.F. Zhang, S.D. Wu, S.X. Li, Combined effects of crystallographic orientation, stacking fault energy and grain size on deformation twinning in fcc crystals, Philosophical Magazine 88 (2008) 3011–3029. https://doi.org/10.1080/14786430802438168.

[62] S. Antonov, M. Detrois, D. Isheim, D. Seidman, R.C. Helmink, R.L. Goetz, E. Sun, S. Tin, Comparison of thermodynamic database models and APT data for strength modeling in high Nb content γ–γ′ Ni-base superalloys, Mater Des 86 (2015) 649–655. https://doi.org/10.1016/j.matdes.2015.07.171.

[63] C.R. LaRosa, M. Shih, C. Varvenne, M. Ghazisaeidi, Solid solution strengthening theories of high-entropy alloys, Mater Charact 151 (2019) 310–317. https://doi.org/10.1016/j.matchar.2019.02.034.

[64] S. Antonov, B. Li, B. Gault, Q. Tan, The effect of solute segregation to deformation twin boundaries on the electrical resistivity of a single-phase superalloy, Scr Mater 186 (2020) 208–212. https://doi.org/https://doi.org/10.1016/j.scriptamat.2020.05.035.

[65] P. Kontis, Z. Li, D.M. Collins, J. Cormier, D. Raabe, B. Gault, The effect of chromium and cobalt segregation at dislocations on nickel-based superalloys, Scr Mater 145 (2018) 76–80. https://doi.org/10.1016/j.scriptamat.2017.10.005.

[66] D. Hull, D.J. Bacon, Introduction to Dislocations, Elsevier, 2011. https://doi.org/10.1016/C2009-0-64358-0.

[67] M. Herbig, M. Kuzmina, C. Haase, R.K.W. Marceau, I. Gutierrez-Urrutia, D. Haley, D.A. Molodov, P. Choi, D. Raabe, Grain boundary segregation in Fe–Mn–C twinning-induced plasticity steels studied by correlative electron backscatter diffraction and atom probe tomography, Acta Mater 83 (2015) 37–47. https://doi.org/10.1016/j.actamat.2014.09.041.

[68] A.S. Ebner, S. Jakob, H. Clemens, R. Pippan, V. Maier-Kiener, S. He, W. Ecker, D. Scheiber, V.I. Razumovskiy, Grain boundary segregation in Ni-base alloys: A combined

atom probe tomography and first principles study, Acta Mater 221 (2021) 117354. https://doi.org/10.1016/j.actamat.2021.117354.

[69] P. Thoudden-Sukumar, Z. Kloenne, S.M. Das, Y. Zheng, H.L. Fraser, B. Gault, S. Antonov, Mechanisms of grain boundary α precipitation in the metastable β-titanium Ti-5Al-5Mo-5V-3Cr, Acta Mater 272 (2024) 119955. https://doi.org/10.1016/j.actamat.2024.119955.

[70] Y. Tomokiyo, K. Kaku, T. Eguchi, The Influence of Solute Atoms on the Stacking Fault Energy in &alpha;Cu&ndash;Al Alloys, Transactions of the Japan Institute of Metals 15 (1974) 39–45. https://doi.org/10.2320/matertrans1960.15.39.

[71] R. deWit, R.E. Howard, Relation of the stacking fault energy to segregation at stacking faults and to the occurrence of phase boundaries in f.c.c. binary alloys, Acta Metallurgica 13 (1965) 655–661. https://doi.org/10.1016/0001-6160(65)90128-8.

[72] X. Zhou, X. Yu, T. Kaub, R.L. Martens, G.B. Thompson, Grain Boundary Specific Segregation in Nanocrystalline Fe(Cr), Sci Rep 6 (2016) 34642. https://doi.org/10.1038/srep34642.

[73] K. Ming, X. Bi, J. Wang, Segregation of Mo atoms into stacking faults in CrFeCoNiMo alloy, Philosophical Magazine 99 (2019) 1014–1024. https://doi.org/10.1080/14786435.2019.1569768.

[74] Y. Xia, S. Lyu, W. Li, Y. Chen, A.H.W. Ngan, Defect-induced inhomogeneous atomic environments in complex concentrated alloys, Int J Plast 169 (2023) 103719. https://doi.org/10.1016/j.ijplas.2023.103719.

[75] S.R. Spurgeon, Y. Du, S.A. Chambers, Measurement Error in Atomic-Scale Scanning Transmission Electron Microscopy—Energy-Dispersive X-Ray Spectroscopy (STEM-EDS) Mapping of a Model Oxide Interface, Microscopy and Microanalysis 23 (2017) 513–517. https://doi.org/10.1017/S1431927617000368.

[76] E.O. Hall, The Deformation and Ageing of Mild Steel: III Discussion of Results, Proceedings of the Physical Society. Section B 64 (1951) 747–753. https://doi.org/10.1088/0370-1301/64/9/303.

[77] N.J. Petch, The Cleavage Strength of Polycrystals, J. Iron Steel Inst. 174 (1953) 25–28.

[78] S. Yoshida, T. Bhattacharjee, Y. Bai, N. Tsuji, Friction stress and Hall-Petch relationship in CoCrNi equi-atomic medium entropy alloy processed by severe plastic deformation and subsequent annealing, Scr Mater 134 (2017) 33–36. https://doi.org/10.1016/j.scriptamat.2017.02.042.

[79] S. Yoshida, T. Ikeuchi, T. Bhattacharjee, Y. Bai, A. Shibata, N. Tsuji, Effect of elemental combination on friction stress and Hall-Petch relationship in face-centered cubic high / medium entropy alloys, Acta Mater 171 (2019) 201–215. https://doi.org/10.1016/j.actamat.2019.04.017.

[80] Q.J. Li, H. Sheng, E. Ma, Strengthening in multi-principal element alloys with local-chemical-order roughened dislocation pathways, Nat Commun 10 (2019) 1–11. https://doi.org/10.1038/s41467-019-11464-7.

[81] N.L. Okamoto, K. Yuge, K. Tanaka, H. Inui, E.P. George, Atomic displacement in the CrMnFeCoNi high-entropy alloy – A scaling factor to predict solid solution strengthening, AIP Adv 6 (2016) 125008. https://doi.org/10.1063/1.4971371.

[82] Z. Wang, Y. Huang, Y. Yang, J. Wang, C.T. Liu, Atomic-size effect and solid solubility of multicomponent alloys, Scr Mater 94 (2015) 28–31. https://doi.org/10.1016/j.scriptamat.2014.09.010.

[83] Y. Zhang, Y.J. Zhou, J.P. Lin, G.L. Chen, P.K. Liaw, Solid-Solution Phase Formation Rules for Multi-component Alloys, Adv Eng Mater 10 (2008) 534–538. https://doi.org/10.1002/adem.200700240.

[84] H.S. Oh, K. Odbadrakh, Y. Ikeda, S. Mu, F. Körmann, C.-J. Sun, H.S. Ahn, K.N. Yoon, D. Ma, C.C. Tasan, T. Egami, E.S. Park, Element-resolved local lattice distortion in complex concentrated alloys: An observable signature of electronic effects, Acta Mater 216 (2021) 117135. https://doi.org/10.1016/j.actamat.2021.117135.

[85] H.S. Oh, S.J. Kim, K. Odbadrakh, W.H. Ryu, K.N. Yoon, S. Mu, F. Körmann, Y. Ikeda, C.C. Tasan, D. Raabe, T. Egami, E.S. Park, Engineering atomic-level complexity in high-entropy and complex concentrated alloys, Nat Commun 10 (2019) 2090. https://doi.org/10.1038/s41467-019-10012-7.

[86] Z. Pei, B. Dutta, F. Körmann, M. Chen, Hidden Effects of Negative Stacking Fault Energies in Complex Concentrated Alloys, Phys Rev Lett 126 (2021) 255502. https://doi.org/10.1103/PhysRevLett.126.255502.

[87] Y.H. Zhang, Y. Zhuang, A. Hu, J.J. Kai, C.T. Liu, The origin of negative stacking fault energies and nano-twin formation in face-centered cubic high entropy alloys, Scr Mater 130 (2017) 96–99. https://doi.org/10.1016/j.scriptamat.2016.11.014.

[88] W. Guo, Z. Pei, X. Sang, J.D. Poplawsky, S. Bruschi, J. Qu, D. Raabe, H. Bei, Shape-preserving machining produces gradient nanolaminate medium entropy alloys with high strain hardening capability, Acta Mater 170 (2019) 176–186. https://doi.org/10.1016/j.actamat.2019.03.024.

[89] X. Wang, R.R. De Vecchis, C. Li, H. Zhang, X. Hu, S. Sridar, Y. Wang, W. Chen, W. Xiong, Design metastability in high-entropy alloys by tailoring unstable fault energies, Sci Adv 8 (2022). https://doi.org/10.1126/sciadv.abo7333.

[90] X.D. Xu, P. Liu, Z. Tang, A. Hirata, S.X. Song, T.G. Nieh, P.K. Liaw, C.T. Liu, M.W. Chen, Transmission electron microscopy characterization of dislocation structure in a face-centered cubic high-entropy alloy Al0.1CoCrFeNi, Acta Mater 144 (2018) 107–115. https://doi.org/10.1016/j.actamat.2017.10.050.

[91] T. Paulauskas, C. Buurma, E. Colegrove, B. Stafford, Z. Guo, M.K.Y. Chan, C. Sun, M.J. Kim, S. Sivananthan, R.F. Klie, Atomic scale study of polar Lomer–Cottrell and Hirth lock dislocation cores in CdTe, Acta Crystallogr A Found Adv 70 (2014) 524–531. https://doi.org/10.1107/S2053273314019639.

[92] L. Qi, C.Q. Liu, H.W. Chen, J.F. Nie, Atomic scale characterization of complex stacking faults and their configurations in cold deformed Fe42Mn38Co10Cr10 high-entropy alloy, Acta Mater 199 (2020) 649–668. https://doi.org/10.1016/j.actamat.2020.07.070.

[93] M. Kolbe, A. Dlouhy, G. Eggeler, Dislocation reactions at γ/γ′-interfaces during shear creep deformation in the macroscopic crystallographic shear system (001)[110] of CMSX6 superalloy single crystals at 1025°C, Materials Science and Engineering: A 246 (1998) 133–142. https://doi.org/10.1016/S0921-5093(97)00733-8.

[94] Q. Li, J.W. Mo, S.H. Ma, F.H. Duan, Y.L. Zhao, S.F. Liu, W.H. Liu, S.J. Zhao, C.T. Liu, P.K. Liaw, T. Yang, Defeating hydrogen-induced grain-boundary embrittlement via triggering unusual interfacial segregation in FeCrCoNi-type high-entropy alloys, Acta Mater 241 (2022) 118410. https://doi.org/10.1016/j.actamat.2022.118410.

[95] H. Li, H. Zong, S. Li, S. Jin, Y. Chen, M.J. Cabral, B. Chen, Q. Huang, Y. Chen, Y. Ren, K. Yu, S. Han, X. Ding, G. Sha, J. Lian, X. Liao, E. Ma, J. Sun, Uniting tensile ductility

with ultrahigh strength via composition undulation, Nature 604 (2022) 273–279. https://doi.org/10.1038/s41586-022-04459-w.

[96] Y. Zeng, X. Cai, M. Koslowski, Effects of the stacking fault energy fluctuations on the strengthening of alloys, Acta Mater 164 (2019) 1–11. https://doi.org/10.1016/j.actamat.2018.09.066.

[97] M. Shih, J. Miao, M. Mills, M. Ghazisaeidi, Stacking fault energy in concentrated alloys, Nat Commun 12 (2021) 3590. https://doi.org/10.1038/s41467-021-23860-z.

[98] A. Jarlöv, W. Ji, R. Babicheva, Y. Tian, Z. Hu, H.L. Seet, L. Tan, F. Liu, Y. Liu, M.L.S. Nai, U. Ramamurty, K. Zhou, Tailoring short-range order and dislocation evolution in Cr–Co–Ni medium-entropy alloys: A molecular dynamics study, Mater Des 240 (2024) 112840. https://doi.org/10.1016/j.matdes.2024.112840.

[99] D.M.C. Nicholson, R.H. Brown, Electrical resistivity of Ni0.8Mo0.2: Explanation of anomalous behavior in short-range ordered alloys, Phys Rev Lett 70 (1993) 3311–3314. https://doi.org/10.1103/PhysRevLett.70.3311.

[100] R.H. Banerjee, A. Arya, H. Donthula, C. Nayak, D. Bhattacharya, S. Banerjee, Quantitative description of the role of Cr on the ordering characteristics of a single phase Ni-16 wt.% Mo- 7wt.% Cr alloy, Acta Mater 219 (2021) 117263. https://doi.org/10.1016/j.actamat.2021.117263.

[101] L. Li, Z. Chen, S. Kuroiwa, M. Ito, K. Yuge, K. Kishida, H. Tanimoto, Y. Yu, H. Inui, E.P. George, Evolution of short-range order and its effects on the plastic deformation behavior of single crystals of the equiatomic Cr-Co-Ni medium-entropy alloy, Acta Mater 243 (2023) 118537. https://doi.org/10.1016/j.actamat.2022.118537.

[102] X. Yang, Y. Xi, C. He, H. Chen, X. Zhang, S. Tu, Chemical short-range order strengthening mechanism in CoCrNi medium-entropy alloy under nanoindentation, Scr Mater 209 (2022) 114364. https://doi.org/10.1016/j.scriptamat.2021.114364.

[103] C.G. Schön, On short-range order strengthening and its role in high-entropy alloys, Scr Mater 196 (2021) 113754. https://doi.org/10.1016/j.scriptamat.2021.113754.

[104] Y.Z. Tian, Y. Bai, L.J. Zhao, S. Gao, H.K. Yang, A. Shibata, Z.F. Zhang, N. Tsuji, A novel ultrafine-grained Fe 22Mn 0.6C TWIP steel with superior strength and ductility, Mater Charact 126 (2017) 74–80. https://doi.org/10.1016/j.matchar.2016.12.026.

[105] D. Wei, X. Li, J. Jiang, W. Heng, Y. Koizumi, W.-M. Choi, B.-J. Lee, H.S. Kim, H. Kato, A. Chiba, Novel Co-rich high performance twinning-induced plasticity (TWIP) and transformation-induced plasticity (TRIP) high-entropy alloys, Scr Mater 165 (2019) 39–43. https://doi.org/10.1016/j.scriptamat.2019.02.018.

[106] W. Fang, R. Chang, X. Zhang, P. Ji, X. Wang, B. Liu, J. Li, X. He, X. Qu, F. Yin, Effects of Cobalt on the structure and mechanical behavior of non-equal molar CoxFe50−xCr25Ni25 high entropy alloys, Materials Science and Engineering: A 723 (2018) 221–228. https://doi.org/10.1016/j.msea.2018.01.029.

[107] R. Chang, W. Fang, X. Bai, C. Xia, X. Zhang, H. Yu, B. Liu, F. Yin, Effects of tungsten additions on the microstructure and mechanical properties of CoCrNi medium entropy alloys, J Alloys Compd 790 (2019) 732–743. https://doi.org/10.1016/j.jallcom.2019.03.235.

[108] D. Wei, X. Li, W. Heng, Y. Koizumi, F. He, W.-M. Choi, B.-J. Lee, H.S. Kim, H. Kato, A. Chiba, Novel Co-rich high entropy alloys with superior tensile properties, Mater Res Lett 7 (2019) 82–88. https://doi.org/10.1080/21663831.2018.1553803.

[109] Z. Li, C.C. Tasan, K.G. Pradeep, D. Raabe, A TRIP-assisted dual-phase high-entropy alloy: Grain size and phase fraction effects on deformation behavior, Acta Mater 131 (2017) 323–335. https://doi.org/10.1016/j.actamat.2017.03.069.

[110] S.F. Liu, Y. Wu, H.T. Wang, W.T. Lin, Y.Y. Shang, J.B. Liu, K. An, X.J. Liu, H. Wang, Z.P. Lu, Transformation-reinforced high-entropy alloys with superior mechanical properties via tailoring stacking fault energy, J Alloys Compd 792 (2019) 444–455. https://doi.org/10.1016/j.jallcom.2019.04.035.

[111] Z. Li, F. Körmann, B. Grabowski, J. Neugebauer, D. Raabe, Ab initio assisted design of quinary dual-phase high-entropy alloys with transformation-induced plasticity, Acta Mater 136 (2017) 262–270. https://doi.org/10.1016/j.actamat.2017.07.023.

[112] Z. Li, K.G. Pradeep, Y. Deng, D. Raabe, C.C. Tasan, Metastable high-entropy dual-phase alloys overcome the strength–ductility trade-off, Nature 534 (2016) 227–230. https://doi.org/10.1038/nature17981.

[113] J.-E. Jin, Y.-K. Lee, Effects of Al on microstructure and tensile properties of C-bearing high Mn TWIP steel, Acta Mater 60 (2012) 1680–1688. https://doi.org/10.1016/j.actamat.2011.12.004.

[114] Y. Bai, Y. Tian, S. Gao, A. Shibata, N. Tsuji, Hydrogen embrittlement behaviors of ultrafine-grained 22Mn–0.6C austenitic twinning induced plasticity steel, J Mater Res 32 (2017) 4592–4604. https://doi.org/10.1557/jmr.2017.351.

[115] Y. Bai, H. Kitamura, S. Gao, Y. Tian, N. Park, M. Park, H. Adachi, A. Shibata, M. Sato, M. Murayama, N. Tsuji, Unique transition of yielding mechanism and unexpected activation of deformation twinning in ultrafine grained Fe-31Mn-3Al-3Si alloy, Sci Rep 11 (2021) 15870. https://doi.org/10.1038/s41598-021-94800-6.